Experiments in Fluids (2026) 67:50
https://doi.org/10.1007/s00348-026-04195-1

RESEARCH ARTICLE

Thermal marking measurements of horizontal velocity gradients, turbulent kinetic energy, and its dissipation rate at an undulating wind ruffled air-water interface

Shantanu Soumya[1] · Nathan Laxague[1] · Ivan Savelyev[2] · Christopher Zappa[3]

Received: 19 August 2025 / Revised: 6 February 2026 / Accepted: 14 February 2026

Abstract
Velocity gradients are critical drivers of turbulent and scalar exchange processes within fluids. Calculating these gradients at a wavy air-water interface presents significant challenges, requiring simultaneous spatially distributed measurements of velocity fields across an undulating interface. In this study, we employ thermal marking velocimetry (TMV), an unobtrusive active velocimetry technique, to capture the surface velocity field over an unstructured grid. The surface velocity field is then used to compute the horizontal surface velocity gradient; together, these enable calculation of the wave orbital velocity, surface strain, vertical vorticity, and turbulent kinetic energy (TKE). Furthermore, a structure function-based approach is employed to estimate the TKE dissipation rate at the wavy interface. Finally, we calculate the Eulerian vortex force field at the surface, providing a quantitative experimental connection between regions of surface convergence and divergence to spanwise variation in the vertical vorticity. These measurement capabilities are important for deepening our understanding of the physical processes governing energy flux across the air-sea interface.

1 Introduction

A turbulent structure's formation, evolution, and dissipation near the surface of a gravity wave ruffled by wind forcing is a result of competing effects between kinematic surface constraints (Guo and Shen 2010), the strain induced due to propagating surface wave, and the mean shear current (Teixeira and Belcher 2002). Kinematic constraints of the free surface lead to the "blockage" effect. As the influence of the free surface grows, the blockage effect amplifies the vertical and horizontal velocity gradient. Turbulent velocity fluctuations near the surface relative to homogenous and isotropic conditions are damped in vertical direction and amplified in the horizontal direction (Guo and Shen 2010). Surface waves interact with turbulent structures through two main mechanisms: (1) direct straining due to the wave's orbital velocity $O(ak\sigma)$, due to correlation between wave strain and turbulent fluctuations, and (2) by the action of Stokes drift, $O(a^2k^2\sigma)$, which has a second-order effect in wave slope. However, the cumulative effect of the second-order Stokes drift over multiple wave cycles is $O(a^2k^2\sigma t)$, which acts to tilt a near-surface vertical eddy along the wave's propagating direction (Teixeira and Belcher 2002; Guo and Shen 2013), where t is time. The presence of wind above the free surface imparts non-zero surface stress. The momentum transferred from wind to growing waves is partitioned between wave growth (Donelan et al. 2006) and surface current via viscous stress (Banner and Peirson 1998). Wave breaking has a significant impact on surface dynamics as it limits wave growth by depositing wave energy into the turbulent current field (Zappa et al. 2007; Hogan et al. 2025). A breaking wave adds a significant fraction of turbulent energy into the flow

Nathan Laxague, Ivan Savelyev and Christopher Zappa contributed equally to this work.

✉ Shantanu Soumya
Shantanu.Soumya@unh.edu

✉ Nathan Laxague
Nathan.Laxague@unh.edu

Ivan Savelyev
ivan.b.savelyev.civ@us.navy.mil

Christopher Zappa
zappa@ldeo.columbia.edu

1 Department of Mechanical Engineering, University of New Hampshire, 105 Main St, Durham, NH 03824, USA

2 U.S. Naval Research Laboratory, Washington, DC 20375, USA

3 Lamont-Doherty Earth Observatory, Columbia University, 61 Rte 9W, Palisades, New York 10964, USA

Published online: 06 April 2026

field, which remains localized within the upper few meters of the surface (Sullivan et al. 2007; Noh et al. 2004). Furthermore, wave breaking generates strong surface normal vortices, which interact with Stokes drift to transfer streamwise momentum in the spanwise direction (McWILLIAMS et al. 1997; Skyllingstad and Denbo 1995; Sullivan et al. 2007). In the absence of wave-breaking, shear production dominates the turbulence generation mechanism near the surface (Teixeira 2018). Lastly, a finite amplitude surface wave modulates the wind flow, which then modulates the wind imparted tangential viscous stress to be a function of the surface wave's phase profile (Kawai 1982; Buckley et al. 2020).

Sub-surface and near-surface turbulence has been extensively investigated in numerical, lab, and field studies. (Sullivan and McWilliams 2010) The lift-off and breakdown of portions of low-speed, streaky structures near a sheared boundary wall or interface are considered as burst events. Each burst consists of several weaker ejection events (Kline et al. 1967), which have a higher likelihood of forming under wave crests. Further, the elevated local generation of vorticity near the wave crest is a result of peak tangential stress at the wave crest, which thickens the vorticity layer(Okuda 1982) and is consistent with increased TKE (Rashidi et al. 1992; Thais and Magnaudet 1996) and normal, streamwise, and vertical components of the Reynolds stress tensor (Jiang and Street 1991) at wave crests. Turbulent energy flux below a surface wave is observed to be a function of time scale determined by wave strain (Thais and Magnaudet 1996). Energy spectra calculated below a monochromatic surface wave field show that the energy transfer in the inertial subrange is governed by the $k^{-5/3}$ scaling law away from the spectral energy peak at the wave frequency.

Exchange of momentum, heat, and gas is limited by its transfer through the viscous sublayer and the molecular diffusive sublayer. This necessitates an understanding of surface flow field dynamics. The inherent non-stationarity of an undulating measurement plane makes surface measurements logistically challenging. Melville et.al. (1998) imaged tiny glass microspheres with a visible camera, alongside a laser slope gauge, and observed that the generation of streamwise-oriented streaky cells on a wind-driven surface current was closely followed by the appearance of surface waves starting from rest. The organization of the microspheres on the surface was qualitatively similar to the thermal structures observed in surface infrared imagery (Veron and Melville 2001). Passive surface thermal images show features organized as streamwise, stretched, and buoyant “overlapping laminae" plumes, with an upstream head followed by a tail in their thermal wakes at low wind speeds and in the absence of wind waves. These surface thermal structures show significant modulation due to the wave strain upon generation of wind waves (Handler et al. 2001). Breaking of very short wind waves without air entrainment are know as“micro-scale" breakers. These micro-breakers are first observed in infrared images as capillary-gravity wave packets (bore-like crests) on steep wind waves, before evolving into micro-breakers that disrupt the water's thermal boundary layer. The disruption in the thermal boundary layer travels at the dominant wave's phase speed, leaving decaying turbulence in its wake (Zappa et al. 2001). A higher fraction of the water surface covered by the wakes of micro-breaking waves increases the flux of weakly soluble gas across the aqueous mass boundary layer (Zappa et al. 2004).

Leveraging the opacity of water to longwave infrared radiation, Veron et al. (Veron et al. 2008) introduced active thermal marking velocimetry to study the kinematic behavior of a surface wave field in the ocean. A CO_2 laser “printed" seven spots on the ocean surface, which were tracked in time to obtain surface velocity measurements. The study showed that the temporal evolution of surface vorticity and divergence can be tracked by analyzing the distortion of point triplets. Following the demonstration of active thermal marking velocimetry, Veron et al. (2009) further reported that the maxima in turbulence intensity and vorticity slightly lag the maximum surface displacement, a consequence of the shearing effect on turbulence and local stretching of the vortex lines by waves. Savelyev (2018) extended TMV to two-camera stereo thermal marking velocimetry (TMV) to reconstruct the wave shape and study the motion of fluid at the surface. Savelyev et al. (2020) used a planar TMV setup to measure surface dynamics and reported a negative correlation of surface TKE with wave slope at high wind speeds, while a positive correlation at low wind speeds. They hypothesized that the rise of airflow shelters much of the water surface from turbulence produced by wind beyond a critical wave slope. Infrared images of the air-water interface show multiscale coherent thermal structures that can be tracked using normalized cross-correlation between successive frames to obtain uniformly gridded velocity vectors. Chickadel et al. (2011) calculated the TKE dissipation rate using cross-correlation between successive infrared images of the surface thermal structure at a river channel flow via the velocity spectral fitting technique. Sutherland et al. (2015) performed thermal stereo imaging of the undulating interface and partitioned the velocity field into rotational and irrotational components. They inferred the TKE dissipation rate at the interface by fitting the vorticity spectrum of the rotational velocity field to a classic vorticity spectrum. Advection of thermal structures can be used to obtain three-dimensional wave-number-frequency spectra of surface temperature fields. The advection of “frozen" turbulent eddies shows up as a linear surface in the wave-number-frequency spectrum, discernible from the dispersion relation surface. The slope of the linear feature in the wave number frequency domain gives the velocity and direction of advective turbulent thermal features (Dugan and Piotrowski 2012;

Brumer et al. 2016). Laxague et al. (2020) used advecting thermal features to obtain the mean velocity at the ocean surface in an interface-following reference frame. Together with a depth-varying mean velocity profile below the surface as obtained by short-wave Doppler shift, they obtained a complete mean velocity profile within the upper few centimeters of ocean.

In this work, we utilize the opacity of water for long-wave infrared radiation to make non-intrusive thermal tracers arranged horizontally as a uniformly spaced grid within the interface's viscous sub-layer ($O \sim 20 - 35\mu m$) from the surface (Downing and Williams 1975). We present experimental design and conditions in Sect. 2. Further, we report our analysis method for tracking the evolution of thermal markers in the viscous sublayer. This tracking technique yields an unstructured grid of Lagrangian velocity measurements at the air-water interface. The unstructured nature of this measurement necessitates a novel approach for determining velocity gradients and for estimating the TKE dissipation. In Sect. 3, we present the phase conditional ensemble, span, and time-averaged surface velocity, strain, turbulent kinetic energy intensity, and dissipation rate as a function of the dominant gravity wave's phase. In Sect. 4, we identify the effect of vortex force on the organization of thermal structures on the air-water interface.

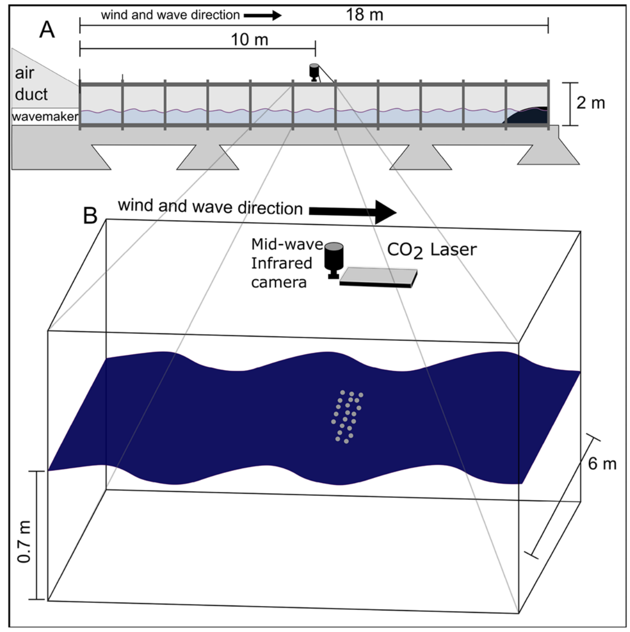

Fig. 1 SUSTAIN wind wave tank schematic and a zoomed view showing placement of the TMV camera and thermal marking laser.

2 Method

2.1 Experiment overview

We conducted the laboratory observations for this work in the Surge-Structure-Atmosphere-Interaction (SUSTAIN) facility at the University of Miami Rosenstiel School of Marine and Earth Atmospheric Science. The working section of the wind-wave tunnel spans 18 m long (streamwise or x direction), 6 m wide (spanwise or y direction), and 2 m high (vertical or z direction). The tunnel was filled with fresh water up to 70 cm. The upstream end of the wind-wave tunnel houses a mechanical wave generator in the lower half of the vertical span that generates surface gravity waves under a range of conditions. The top half of the upstream end served as an inlet for wind in the tunnel's test section. The downstream end of the tunnel is fitted with a beach in the lower half, minimizing any residual reflections, while the exit vents (an open-loop wind tunnel system) allow the oncoming wind to be ejected.

2.1.1 Sensors used

Measurements relevant to this work were performed using an active thermal marking system, a three-dimensional sonic anemometer manufactured by Campbell Scientific, which measured wind speed 65 cm from the interface at 20 Hz, and an Ultrasonic Distance Measure (UDM). The active thermal marking system consists of a cooled mid-wave infrared camera (FLIR X8500sc) and a CO_2 laser (Synrad, Pulstar p100) fitted with a programmable marking head (FH Flyer). The CO_2 laser emits radiation with an average power of 100 W in the long-wave infrared range of 10.6 μm. This operating wavelength makes the water surface opaque to the emitted laser beam. The laser deposits its energy as heat within the top few microns ($O \sim 20 - 35\mu m$) of the water column for the IR camera to detect. A cooled mid-wave ($3.0 - 5.0\mu$m) infrared camera (FLIR X8500sc) was used to track the advection and distortion of thermal markings. The camera was oriented nadir to the air-water interface at quiescent conditions, as shown in Fig. 1. The infrared camera had a sensor resolution of 1280 × 1024 pixels, thermal sensitivity ≤ 20 mK, and an integration time of 3 ms (Savelyev and Fuchs 2018). We used a 17 mm focal length FLIR infrared lens for this work, which, at 1.3 meters from the measurement plane, had a field of view covering 1.023 m in the streamwise direction and 1.28 m in the spanwise direction at the calibration plane. The laser housing has two lightweight scan mirrors that can change the 2D beam angle orientation at a rate exceeding 1 kHz. These programmable mirrors are controlled using WinMark Pro v6, which allows users to create laser patterns or import externally created patterns in image format (Savelyev and Fuchs 2018). For this work, we used an evenly spaced grid of dots, with the heated spot's diameter averaging about 1.35 cm at the air-water interface and the neighboring spot's centroid separation averaging 5.5 cm. The thermal spots were marked using the CO_2 laser, which acted as tracers to obtain surface velocity measurements at the air-water interface. Additionally, three Senix Tough sonic-50 UDMs at 15 m fetch provided independent surface elevation measurements of the wavy interface. The UDM had a maximum range of 15 meters and a dead band of 3 cm. The UDMs recorded water surface elevation at 20 Hz. Wind velocity measured by the sonic anemometer at 65 cm was extrapolated to 10 m reference height and reported as U_{10} assuming the logarithmic profile and neutral thermodynamic conditions for every run in Table 1.

2.1.2 Experimental conditions

The experiments were conducted over seven days in Fall 2022. The open-loop wind tunnel system used ambient wind, thus rendering surface heat flux from the air-water interface a function of time. On days 2, 4, and 6 of the experiment, the water was heated to 34 $^\circ C$ at the start of the experiment, which, due to natural convection and conduction, cooled to 25 $^\circ C$ during the day's proceedings. At the beginning of day 3, we cooled the water to 16 $^\circ C$, which, during the day's measurements, heated back to 20 $^\circ C$. On days 1, 5, and 7, measurements were started at the equilibrium temperature and showed no significant deviation in water temperature throughout the day.

Mechanical waves of amplitude 2 cm, 4 cm, and 6 cm were generated using an array of mechanical pedals at 0.58 Hz (σ_w). These surface-propagating gravity-scale waves had a wavelength (λ = 3.8 m), wavenumber (k = 1.65 rad/m), and group velocity (C_g = 1.61 m/s). For each wave amplitude, the wind fan was operated at three different variable-frequency drives, which generated mean reference wind speed (U_{10}) of 5.3 m/s, 8.05 m/s, and 10.2 m/s. Deviation from the small amplitude (or slope) assumption from the mean water level of the surface on which the cylindrical wave's governing equation is being solved necessitates the inclusion of higher-order correction terms to the first-order solution. Figure 2 shows the classification of all experimental conditions plotted on top of the validity regime of different orders (including higher order terms) solutions to the cylindrical wave equation (Méhauté 1976). Figure 2 suggests a third-order weakly non-linear theoretical solution can appropriately represent the gravity scale waves considered in this study.

A summary of environmental conditions for all runs studied in this work, alongside relevant bulk environmental and flow parameters are presented in Table 1.

2.2 TMV data processing

Each recording of the spatiotemporal evolution of the interface was six minutes long, split into one minute of passive infrared recording followed by five minutes of active thermal marking records. The FLIR8500sc thermal imaging camera recorded oncoming mid-wave infrared radiation as 14-bit grayscale intensity for each of 1023 × 1280 pixels in the focal plane array.

2.2.1 Spatial calibration and lens distortion correction

A floating checkerboard calibration target was placed on the water surface within the camera's field of view in quiescent conditions. Slight drift of the calibration target during acquisition was corrected via a two-dimensional cross-correlation of the checkerboard pattern between consecutive images. The drift-corrected images were then checked for possible rotation of the checkerboard during acquisition. A sensitivity study was conducted to test for possible checkerboard rotation. The study involved rotating an image within a fixed range of $[-2^\circ, 0.1^\circ, 2^\circ]$. The results indicated that the smallest pixel count for the checkerboard size was observed at a 0° rotation angle. This suggests that the calibration plate did not rotate relative to the camera during calibration image acquisition. The resulting images were averaged over ten frames. Comparing the number of camera pixels required for thermal imaging of a single checker directly provided a spatial calibration of 1 mm per pixel at the still-water level. This process was repeated at the frame's center and fringes, and the calibration factor was found to be remarkably consistent.

2.2.2 Spot detection

The 14-bit grayscale thermal images had multiple noise sources, and the use of a decaying tracker (actively marked thermal spots) to obtain surface velocimetry introduced several propagative errors. The two broad categories of potential measurement error sources were treated in a two-step quality control process. First, a preprocessing filter was designed to treat sources of noise and contrast stretch actively marked spots from background thermal noise and subtract reflections from stationary sources, as discussed in Sect. 2.2.3. In the second step, a velocimetry quality control was performed to remove sources of error due to the dissipative nature of the actively marked spots discussed in Sect. 2.2.4

2.2.3 Image pre-processing

The observed noise in the grayscale images was caused by static thermal sources and reflectors in the vicinity of the measurement plane and a temporally evolving surface thermal signature that advected in time. Additionally, significant variation in water temperature across different runs necessitated pre-processing to isolate the actively marked spots.

The primary motivation for pre-processing is to suppress background radiation and enhance the contrast of the actively marked spots relative to it. The minute-long passive infrared

Table 1 Summary of all processed runs with third ($a_{\text{fit}}^{\text{3rd}}$), second ($a_{\text{fit}}^{\text{2nd}}$) and first ($a_{\text{fit}}^{\text{linear}}$) order amplitude fit of the Stokes solution to measured velocity, wind speed (U_{10}), air friction velocity (u_{air}^{*}), interface temperature (T_{w}), air temperature (T_{a}), relative humidity (RH), and turbulent kinetic energy (q_{x}^2, q_{y}^2).

Run	$a_{\text{fit}}^{\text{3rd}}$ [cm]	$a_{\text{fit}}^{\text{2nd}}$ [cm]	$a_{\text{fit}}^{\text{linear}}$ [cm]	U_{10} [m/s]	$u*_{\text{air}}$ [m/s]	T_{w} [°C]	T_{a} [°C]	RH [%]	q_x^2 [cm^2/s^2]	q_y^2 [cm^2/s^2]
001	6.27	6.19	5.80						11.241	4.971
002	4.05	4.02	3.85						13.547	5.106
003	2.46	2.45	2.18						13.285	4.947
004	4.10	4.05	3.79						7.297	2.434
005	1.95	1.95	1.97						8.636	2.118
006	6.47	6.34	5.65						3.799	1.602
007	4.11	4.08	3.75						4.765	0.899
008	1.96	1.95	1.89						2.794	0.430
009	0	0	0	8.0	0.180		30.47	75.2	8.970	2.737
010	0	0	0	5.2	0.070		31.21	77.6	4.199	0.117
011	0	0	0	10.3	0.303		31.25	82.0	23.728	10.129
012	0	0	0	8.1	0.178		31.60	87.2	8.814	2.271
013	0	0	0	5.3	0.069		31.64	87.0	10.155	0.178
014	0	0	0	5.4	0.069		30.11	68.2	2.356	0.057
015	0	0	0	8.2	0.176	33.45	30.76	67.2	20.367	1.712
016	0	0	0	10.4	0.304	33.12	31.16	68.2	48.938	8.395
017	1.97	1.97	1.89	10.3	0.303	33.05	31.18	72.2	10.823	3.092
018	4.14	4.09	3.78	10.2	0.300	32.47	31.06	76.0	8.597	2.731
019	0	0	0	5.3	0.069	16.3	30.88	75.0	36.221	0.547
020	0	0	0	8.0	0.178	16.5	30.87	75	22.495	2.374
021	0	0	0	10.2	0.304	16.9	30.24	75.0	54.223	9.941
022	1.99	1.98	1.83	10.3	0.306	17.3	29.64	75.2	14.705	3.786
023	4.12	4.09	3.78	10.3	0.304	18.2	29.41	77.0	8.841	3.552
024	1.97	1.97	1.89	10.4	0.302	19	31.29	74.8	11.026	6.978
025	4.13	4.09	3.78	10.4	0.302	19.4	31.94	75.0	9.461	5.620
026	1.97	1.97	1.89	8.1	0.035	19.8	31.62	76.0	5.443	2.286
027	4.13	4.09	3.78	8.2	0.176	19.8	31.86	76.2	5.339	2.253
028	1.97	1.97	1.89	10.4	0.302	34.1	31.88	77.6	12.464	6.568
029	4.13	4.09	3.78	10.4	0.302	33.3	31.92	76.4	10.643	5.333
030	1.97	1.97	1.89	7.8	0.178	32.7	30.54	75.2	4.955	1.982
031	4.13	4.09	3.78	8.1	0.178	32.4	30.83	76.2	5.759	2.373
032	0	0	0	9.0	0.275	32.3	31.05	75.40	32.833	8.109
033	0	0	0	8.1	0.176	32	30.95	77.80	12.669	2.029
034	0	0	0	5.3	0.069	31.7	30.96	78.0	11.511	0.198
035	1.97	1.97	1.89	10.3	0.300	31.4	31.13	78.8	11.521	4.268
036	4.13	4.09	3.78	10.3	0.300	30.8	31.14	77.4	9.832	3.968
037	1.97	1.96	1.89	8.1	0.175	22.3	30.93	77.0	6.807	1.935
038	4.11	4.08	3.78	8.2	0.177	22.7	30.55	76.8	6.901	2.252
039	4.12	4.08	3.79	5.2	0.065	22.3	29.85	79.2	1.512	0.635
040	1.97	1.97	1.89	5.2	0.065	22.4	29.29	80.0	0.755	0.357
041	1.97	1.97	1.89	5.4	0.069	22.7	30.40	71.8	1.783	0.391
042	1.97	1.96	1.89	5.3	0.070	23	31.17	73.8	1.416	0.352

Table 1 continued

Run	$a_{\mathrm{fit}}^{\mathrm{3rd}}$ [cm]	$a_{\mathrm{fit}}^{\mathrm{2nd}}$ [cm]	$a_{\mathrm{fit}}^{\mathrm{linear}}$ [cm]	U_{10} [m/s]	$u*_{\mathrm{air}}$ [m/s]	T_{w} [°C]	T_{a} [°C]	RH [%]	q_x^2 [cm^2/s^2]	q_y^2 [cm^2/s^2]
043	4.12	4.08	3.78	5.3	0.068	33.5	31.36	76.0	2.671	0.994
044	6.50	6.36	5.67	10.4	0.300	32.8	31.51	76.6	10.103	4.996
045	6.42	6.30	5.68	8.2	0.177	32.8	31.89	78.6	4.936	2.755
046	6.36	6.26	5.68	5.3	0.068	32.6	32.00	76.0	2.917	1.282
047	1.97	1.97	1.89	5.4	0.068	32.4	32.34	74.6	1.975	0.415
048	4.12	4.08	3.78	5.4	0.069	31.9	32.02	76.2	4.628	0.967
049	6.50	6.36	5.67			31.8			9.492	4.739
050	6.47	6.34	5.68	8.2	0.177	31.6	30.43	78.0	6.121	2.610
051	6.50	6.35	5.68	5.3	0.069	31.6	30.31	77.6	2.525	1.114
052	6.47	6.34	5.53	10.4	0.303	31.5	31.00	72.2	9.976	3.952
053	6.46	6.33	5.63	8.2	0.178	31.1	31.10	73.8	6.916	2.793
054	6.47	6.34	5.60	5.3	0.069	31	30.82	72.2	3.064	1.315

recordings at the beginning of each run provided background mid-wave infrared intensity. A 200-frame median of passive infrared images was subtracted from the original grayscale images to reduce background radiation and reflection from stationary bodies. For measurements performed in warm water, it was necessary to further to contrast-stretch the actively marked spots from the background radiation for the range of heat flux conditions measured. A three-step process was implemented to contrast-stretch the actively marked grayscale images (say image $I_{\mathrm{grayscale}}$). In the first step, a diamond-shaped structuring element was used to first dilate and then erode the original grayscale image. The result of the morphological operation was then subtracted from the original grayscale image to obtain image I_1 ($I_1 = I_{\mathrm{grayscale}} - \mathrm{erosion}(\mathrm{dilation}(I_{\mathrm{grayscale}}))$) using Matlab's morphological filter toolbox's *imtophat*. In the second step, the same structuring element was used to first erode and then dilate the original grayscale image. The result of the morphological operation was then subtracted from the original grayscale image to obtain image I_2 ($I_2 = I_{\mathrm{grayscale}} - \mathrm{dilate}(\mathrm{erode}(I_{\mathrm{grayscale}}))$) using Matlab's morphological filter toolbox's *imbothat*. The final contrast-stretched image was prepared by adding the top-hat filtered image to the grayscale image and subtracting the bottom-hat-filtered image from the added image ($I_{\mathrm{contrast\ stretched}} = I_{\mathrm{grayscale}} + I_1 - I_2$). Figure 3 shows the effect of the above contrast stretching operation. The image on top left shows an unfiltered grayscale image ($I_{\mathrm{grayscale}}$) while the image on top right shows the contrast-stretched image ($I_{\mathrm{contrast\text{-}stretched}}$) in logarithmic scale. Binarized result of the grayscale image ($I_{\mathrm{grayscale}}$) (binarization threshold was $3 \times I_{99}$, where I_{99} is 99th percentile intensity of the median frame) is shown in bottom left panel while the binarized result of the contrast stretched image is shown in bottom right panel. Visual inspection of the binarized image shows a significantly

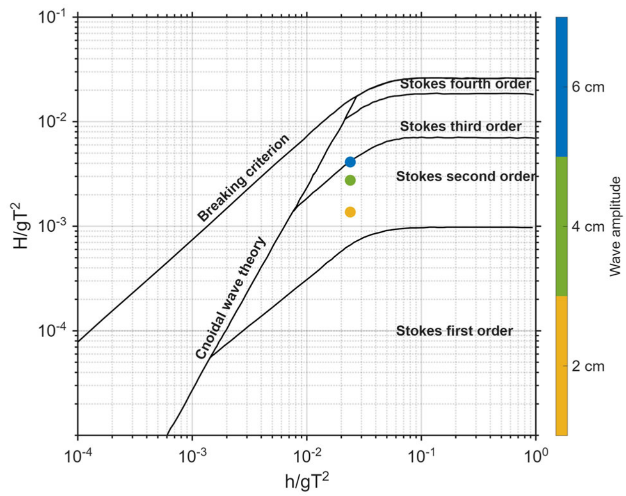

Fig. 2 Classification of mechanically generated wave of wave amplitude 2 cm, 4 cm, and 6 cm at $\sigma = 0.58$ Hz for different order cylindrical wave solution's validity regime (Méhauté 1976). Here, H represents wave height, h represents water depth, T represents wave period and g is gravitational acceleration.

higher number of actively marked spots (marked by red and blue circles; categorization criteria for the red and blue circles are presented in section 2.2.4). The binarized and contrast-stretched grayscale images ($I_{\mathrm{contrast\text{-}stretched}}$) were used to extract the weighted centroid, area, perimeter, and mean intensity of individual spots using MATLAB's standard feature-detection algorithm *regionprops*.

2.2.4 Velocimetry quality control

Even with contrast stretching, the intensity of thermal marks decayed over time. While the surrounding fluid was cooler than the location of actively marked spots, the air-water interface still had its own spatially varying background ther-

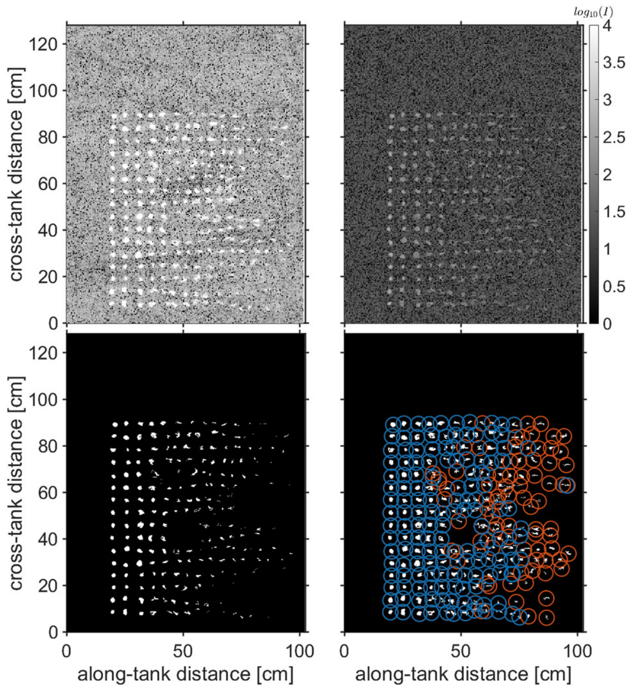

Fig. 3 Figure on top left shows the original grayscale image, and on top right shows the image post sequential top hat filtered image addition and bottom hat filter image removal. The grayscale color map for the top plots is $log_{10}(I)$. A visual inspection of grayscale images shows suppressed background features (top right) compared to the original image (top left). Bottom left panel shows the binarized version of the original grayscale image shown on top left, while the bottom right panel shows the binarized version of the contrast-stretched image shown on top right. Detected bright features in the binary image are encircled. Accepted spots after implementing quality control are circled in blue, while rejected spots are shown in red.

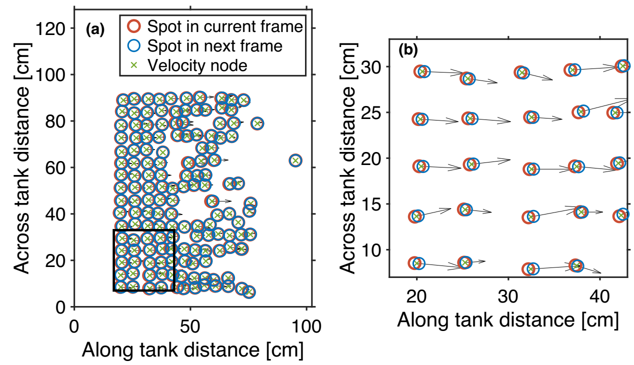

Fig. 4 Panel (**a**) shows the spot location in two consecutive frames. Panel (**b**) shows a zoomed-in view of the region marked by the red box in the top panel. Red circles mark a spot's location in the frame, and a blue circle represents the spot's location in the next frame. The vectors represent the magnitude and direction of the spot's velocity. The green cross represents the location of the node where velocity information is stored.

mal features and signature. Thermal features at the air-water interface advect and evolve due to interface hydrodynamics. These naturally occurring thermal patterns are sustained because the sensible, latent, and longwave radiative fluxes result in a "cool skin" within the upper few microns of the surface, which can be $\sim 0.2-0.5°C$ cooler than the water below it (Fairall et al. 1996). An actively marked spot on the water surface loses its thermal energy to the surrounding fluid due to turbulence and thermal diffusion. A nearby cool skin bright feature can produce a false spot detection as a spot's grayscale intensity decays due to loss of its thermal energy. These false detections resulted in spurious centroid jumps and extreme velocity magnitudes in a spot's otherwise smooth Lagrangian velocity time series. Each spot's Lagrangian time series was analyzed using three criteria to eliminate the transient noise sources. First, spots with a lifetime of 120 ms or less were discarded. Further, the spot lifetime was limited to one second, as the decay of a spot's grayscale intensity increased susceptibility to false detections. Second, an "intensity-based" tracking was performed for every detected spot. In this tracking, the intensity of each spot's first frame of appearance was clustered into three bins using the K-means clustering algorithm (which partitions the dataset into groups by minimizing the distance between data points and their centroids), along with all other detected spots in that frame. An actively marked spot in its first frame of appearance was part of the highest-intensity K-means cluster and exhibited exponential decay over time. Whereas throughout its evolution, the noise remained in the lowest K-means cluster. Finally, for the third criterion, each spot's Lagrangian velocity time series was trimmed at the first occurrence where the spot's instantaneous Lagrangian velocity exceeded three times the standard deviation of the Lagrangian velocity time series. A demonstration of velocimetry quality control is shown in the bottom-right panel of Fig. 3. In this plot, the blue circles mark all accepted spots, while the red circles mark all rejected spots in a frame following the velocimetry quality control discussed above Panel a of Fig. 4 shows the locations of spots in two subsequent frames and its velocity vector, panel b shows a zoomed in view of the region marked with solid black line in panel a.

2.2.5 Surface elevation and slope correction

Planar calibration in quiescent conditions inherently assumes a measurement plane at a fixed distance from the camera. However, the elevation and slope of a wavy measurement plane evolve as a function of space and time. The deviation from the quiescent condition for a 6 cm amplitude wave will over and under-estimate streamwise and spanwise velocity by $\pm 4.616\%$ at the wave crest and wave trough, respectively. While at the steepest positive and negative slope, the velocity vector will be over-and under-estimated by $\pm 0.72\%$. Planar measurements from a single camera pointed directly at the measurement plane cannot estimate the vertical elevation of the wavy measurement plane. However, the first-pass veloc-

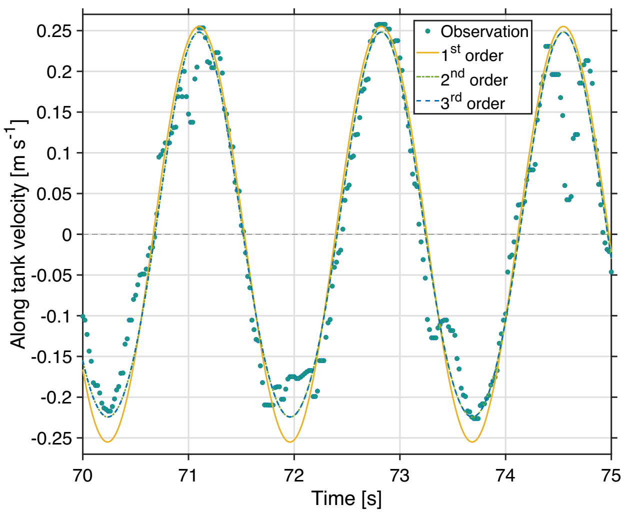

Fig. 5 Frame center velocity measurement and theoretical fit for first, second order and third order velocity fit for experimental condition 6 cm paddle amplitude, 0.58 Hz wave frequency and $U_{10} \approx 10.2$ m/s.

ity measurement on a wavy surface will be dominated by contributions from the surface gravity wave field. Velocity measurements calibrated for quiescent conditions were fitted to the theoretical first, second, and third-order Stokes solution of the cylindrical wave equation (Dingemans 1997). The Eulerian velocity time series was constructed by sampling velocity within a 20 cm window at the frame center. This Eulerian time series was then fitted to the first, second, and third-order theoretical solutions using the least-squares method. The least squares method uses the functional relationship between the fit parameters, as given by the Stokes solution, and iterates over the parameter values to minimize the difference between the theoretical estimates and the observed values. The parameters of the least square fit were wave amplitude ($a_{\text{fit}}^{i^{\text{th}}\text{order}}$), frame center phase offset ($\vartheta_{\text{fit}}^{i^{\text{th}}\text{order}}$) for first-order fit, while amplitude corrected frequency ($\sigma_w^{i^{\text{th}}\text{order}}$), and wave number($k^{i^{\text{th}}\text{order}}$) were additional fit parameters for second and third order (where, $i = 1$, 2 & 3). Figure 5 shows a snippet of the frame center Eulerian velocity time series and its theoretical fit. Using the fit parameter, surface elevation, and slope were estimated for the measurement field and for the recording duration.

Elevation correction, η_{corr}, and surface slope correction, η'_{corr}, is

$$\eta_{\text{corr}} = \frac{Z_{\text{camera}} - (h + \eta_t^{\text{spot}})}{Z_{\text{camera}} - h};$$
$$\eta'_{\text{corr}} = \left\{ \cos\left(\arctan\left(\frac{\partial \eta_t^{\text{spot}}}{\partial x} \right) \right) \right\}^{-1} \tag{1}$$

streamwise and spanwise correction in the velocity field is then given by

$$u_{\text{corrected}} = u \times \eta_{\text{corr}} \times \eta'_{\text{corr}} \tag{2}$$
$$v_{\text{corrected}} = v \times \eta_{\text{corr}} \tag{3}$$

A sensitivity analysis investigating the effect of these corrections at increasing wind speed and wave amplitude showed that the root mean square error (RMSE) between the theoretical streamwise velocity gradient and observed du/dx (du/dx RMSE; Sect. 2.2.6 describes calculation of TMV-derived velocity gradient) improved only slightly relative to the uncorrected measurement. The du/dx RMSE of a 2 cm amplitude wave increased from 0.45 [s^{-1}] at 5.3 m/s (U_{10}), to 0.55 [s^{-1}] at 8.05 m/s (U_{10}), to 0.8 [s^{-1}] at 10.2 m/s (U_{10}). At the highest wind speed 10.2 m/s (U_{10}) change in wave amplitude from 2 cm to 4 cm increased the du/dx RMSE from 0.8 s^{-1} to 0.9 s^{-1}, but reduced to 0.65 s^{-1} for 6 cm amplitude waves.

2.2.6 Unstructured grid velocity gradient

The relative displacement of two adjacent particles in any flow field is given by

$$\mathrm{d}u_i = \left(\frac{\partial u_i}{\partial x_j} \right) \mathrm{d}x_j \tag{4}$$

The velocity gradient tensor within parentheses of equation 4 can be further decomposed into symmetric strain rate $\mathbf{S}_{ij}$ and skew-symmetric rotation rate $\mathbf{R}_{ij}$ tensors:

$$\frac{\partial u_i}{\partial x_j} = \mathbf{S}_{ij} + \mathbf{R}_{ij} \tag{5}$$

$$\text{where } \mathbf{S}_{ij} = \frac{1}{2}\left(\frac{\partial u_i}{\partial x_j} + \frac{\partial u_j}{\partial x_i} \right), \quad \text{and } \mathbf{R}_{ij} = \frac{1}{2}\left(\frac{\partial u_i}{\partial x_j} - \frac{\partial u_j}{\partial x_i} \right) \tag{6}$$

The relative motion of adjacent fluid elements may be described through linear combinations of the velocity gradient tensor components, which can be chosen such that (Rascle et al. 2016):

$$\text{divergence}: \quad \frac{\partial u}{\partial x} + \frac{\partial v}{\partial y} \qquad \text{vorticity}_z: \quad \frac{\partial v}{\partial x} - \frac{\partial u}{\partial y} \tag{7}$$

$$\text{strain}_x: \quad \frac{\partial u}{\partial x} - \frac{\partial v}{\partial y} \qquad \text{shear}_x: \quad \frac{\partial v}{\partial x} + \frac{\partial u}{\partial y} \tag{8}$$

Calculating the velocity gradient of an unstructured-grid velocity field evolving continuously in time required the use of the nearest-neighbor approach. Where each detected spot and its neighboring spots were individually analyzed using two velocity gradient calculation schemes. First, the central difference approach was implemented, in which spots within a circular neighborhood of a central spot were divided into eight bins; the median velocities of opposing bins were subtracted, divided by their separation, and averaged to estimate velocity gradients in the streamwise and spanwise directions. However, the central difference approach performed poorly, achieving 50% of the theoretical estimates. This under estimation is a result of averaging operation in the central difference approach. A different approach was necessary to obtain a reliable surface-velocity-gradient result. "Nearest neighbor velocity linear fit's projection" is used to calculate the first-order surface velocity gradient. The projection method uses the fact that, at any given time, the surface normal vector points in the direction of the steepest change. A linear two dimensional surface may be represented as:

$$z = f(x, y) = Ax + By + D \tag{9}$$

with the surface normal vector at (x_o, y_o), is given by

$$N = \begin{bmatrix} \dfrac{\partial f(x_o, y_o)}{\partial x} \\ \dfrac{\partial f(x_o, y_o)}{\partial y} \\ -1 \end{bmatrix} = \begin{bmatrix} A \\ B \\ -1 \end{bmatrix} \tag{10}$$

A direct comparison between the middle and the rightmost term in equation 10 gives

$$\frac{\partial f}{\partial x} = A \quad and \quad \frac{\partial f}{\partial y} = B \tag{11}$$

Using the least-squares method, a linear two-dimensional fit was calculated about a center spot using the streamwise and spanwise velocities of its nearest neighbors as marked by red circle shown in left panel of Fig. 6. The streamwise velocity fit's surface normal vector was calculated by replacing $f(x, y)$ with $\vec{u}(x, y)$ to get $\frac{\partial u}{\partial x}$ and $\frac{\partial u}{\partial y}$ as shown on the right panel in Fig. 6. While, replacing $f(x, y)$ with $v(x, y)$ gave $\frac{\partial v}{\partial x}$ and $\frac{\partial v}{\partial y}$. Figure 7 shows instantaneous surface divergence (panel a), vorticity(panel b), shear (panel c), and strain (panel d), which were calculated using observed velocity gradient. The magnitude of the surface velocity gradient-derived quantities is normalized by their 99th percentile value. The dashed green line marks the location of the mechanically-generated wave's crest.

2.3 Surface turbulent kinetic energy

Total turbulent kinetic energy (q^2) at the surface can be written as the sum of streamwise velocity variance (q_x^2) and spanwise velocity variance (q_y^2) as shown in Eq. 12 since the turbulent vertical velocity component at the TMV measurement plane is suppressed due to free boundary, where, the streamwise and spanwise TKE is given by equation 13.

$$q^2 = \frac{1}{2}\left(q_x^2 + q_y^2\right) \tag{12}$$

$$q_x^2 = \frac{1}{2}\left(u'^2\right) \quad \text{and} \quad q_y^2 = \frac{1}{2}\left(v'^2\right) \tag{13}$$

Calculating the turbulent velocity fluctuation $u'(x, y, t)$ of the spatial measurement requires removal of the mean $\bar{u}(x)$ and orbital $\widetilde{u}(x, t)$ contributions of the velocity from the instantaneous velocity measurements $u(x, y, t)$. The orbital velocity is a consequence of the surface propagating gravity waves. These orbital velocity components are irrotational; however, rotationality is an essential characteristic of turbulent flows. Thus, for a unidirectional wave, the surface turbulent velocity fluctuation is given by $u'(x, y, t) = u(x, y, t) - \bar{u}(x) - \widetilde{u}(x, t)$ and $v'(x, y, t) = v(x, y, t) - \bar{v}(x)$. Where $\bar{u}(x, y)$ (or $\bar{v}(x, y)$) is the spatial mean, whereas, the $\widetilde{u}(x, t)$ is the surface wave orbital velocity. Due to the unidirectionality of the mechanically generated waves, the orbital velocity has a non-zero contribution to the streamwise current while no contribution in spanwise direction. The nodes of the unidirectional two-dimensional velocity field at any fixed time vary in phase, dependent on the streamwise coordinate. Following Laxague (2020), velocity nodes were sorted within 5° bins according to the node's phase over one wave period $[0, 2\pi)$. The sorting operation is based on the node's phase obtained by fitting frame center velocity to the third-order Stokes solution. At each time stamp, every spot was categorized into 72 phase bins (each with a 5° phase discretization) (Laxague et al. (2020) called these three-dimensional phase-sorted temporal stacks "phasograms"). Within each phase bin, subtraction of the phase bin's mean velocity removed the average and the orbital velocity component from the instantaneous velocity. A similar procedure was used to calculate spanwise velocity fluctuations, in which the mean contribution was removed by subtracting the bin's mean spanwise velocity. Inspection of the spanwise velocity fluctuation showed phase-locked periodic oscillation. This spanwise periodic oscillation could have resulted from two non-operating wave pedals at the edge of the tank, which remained non-operational throughout the experiment. To correct for the phase-locked, periodic, spanwise fluctuating component, a second-order polynomial detrend was applied to the fluctuating velocity field within each phase bin. To maintain uniformity, a second-order polynomial detrend was also applied to every streamwise and spanwise fluctuating velocity phasogram. The phase-sorted velocity fluctuations were then squared and averaged in time to obtain directional turbulent kinetic energy response to the wave shape as a function of varying phase over one wave period for the entire run.

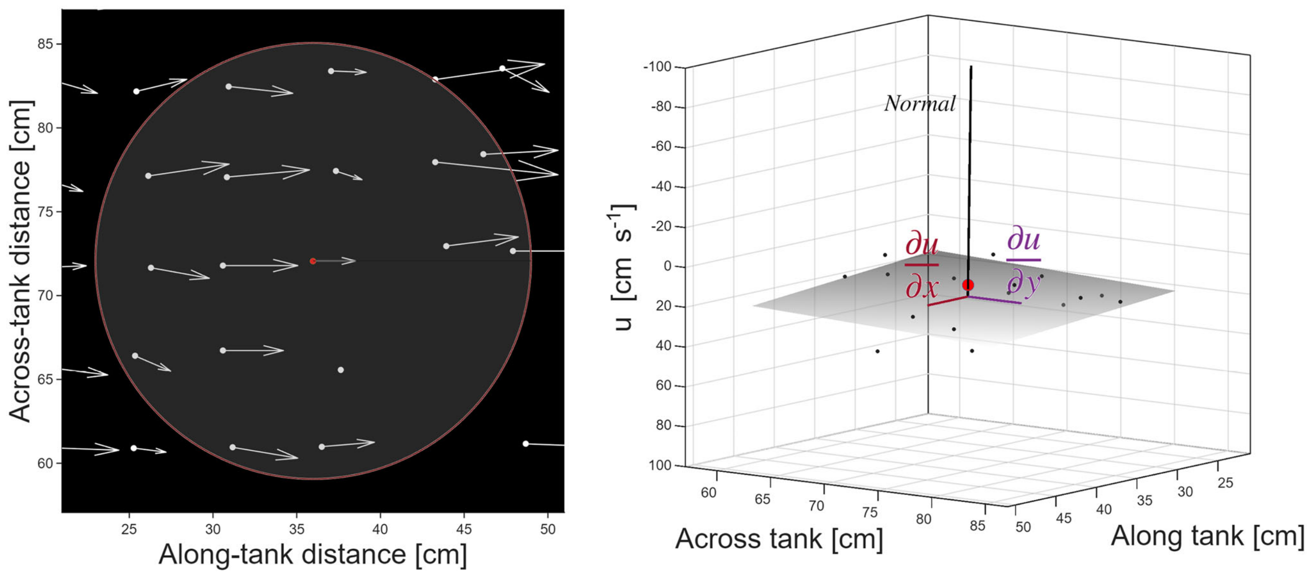

Fig. 6 Panel on left shows a zoomed-in view of the region of interest in a frame. The shaded area shows the region of the nearest neighbor. The panel on the right shows the linear-velocity fit surface and its surface normal in black. The surface normal's projections along and across the tank direction give the velocity gradients in those directions, shown by the blue and red vectors, respectively. Center spot is marked in red.

The second-order detrend operation changed the skewness ($\sim$ 28%) and kurtosis ($\sim$ 19%) of the fluctuating velocity probability density function distribution relative to simple mean (zeroth-order) subtraction.

2.4 Surface turbulent kinetic energy dissipation rate

Direct estimates of the turbulent kinetic energy dissipation rate from velocity derivatives require measuring the velocity field with spatial resolution down to the Kolmogorov scales in the flow of O(<mm). As discussed in section 2.1.1, the spots in actively marked grids were separated by 5.5 cm in the spanwise and streamwise direction. The separation of the actively marked spots limited the smallest resolvable scale in this study to $\sim$ 10 cm. Frequently, experimental estimates of dissipation rates from the velocity field can be obtained by fitting the observed velocity-wave number spectrum to the theoretical wave number spectrum within the constant energy transferring inertial sub-range of semi-empirical homogeneous, isotropic turbulence. However, once marked, the Lagrangian evolution of the actively marked tracers distorts and advects the measurement node's relative position, leading to inconsistent spatial resolution between frames. The unstructured grid limits the use of the spectrum fitting technique for an actively marked dataset. A second-order structure function approach has been successfully used in the past for estimating the near-surface vertical profile of TKE dissipation rate using an Acoustic Doppler Current Profiler (ADCP) (Wiles et al. 2006; Thomson 2012; Guerra and Thomson 2017) and two-dimensional surface turbulence statistics measurements (Baker et al. 2023). Adopting the second-order 1D structure function methodology for the horizontal turbulent velocity field ($u'(y)$ & $v'(y)$) within every 5° phase bin was investigated at every time stamp.

Our measurement depth $\sim 20-35\mu m$ from the interface places our measurement plane within the viscous sublayer of the marine boundary layer. The surface kinematic constraints suppress the vertical turbulent velocity and transport term in the energy equation within the viscous sublayer of the aqueous boundary layer. The absence of the turbulent stretching term within the viscous sublayer (Guo and Shen 2010), make surface turbulence statistically and mechanistically two-dimensional. Dimensional scaling arguments (Kraichnan 1967; Batchelor 1969; Kraichnan 1971), numerical(Boffetta 2007) and ocean surface laboratory measurements within surfzone (Baker et al. 2023) and open ocean (Sutherland and Melville 2015) show the existence of two inertial subranges; first at scales smaller than the forcing scales due to direct enstrophy cascade and second an inverse energy cascade at scales larger than the forcing scales. Simultaneous observations of thermal features and surface slope show that the microbreakers disrupt the skin layer and their propagating front typically spans $O \sim cm$ and advects faster than the surrounding fluid, under mild wind forcing at a fetch comparable to that of this study (Zappa et al. 2001, 2004). The grid markers used in the current work restrict measurements of the direct enstrophy cascade inertial subrange, but are suited for measurements within the inertial subrange of the large-scale inverse cascade range. The second-order structure must have a range of scales uniquely defined by

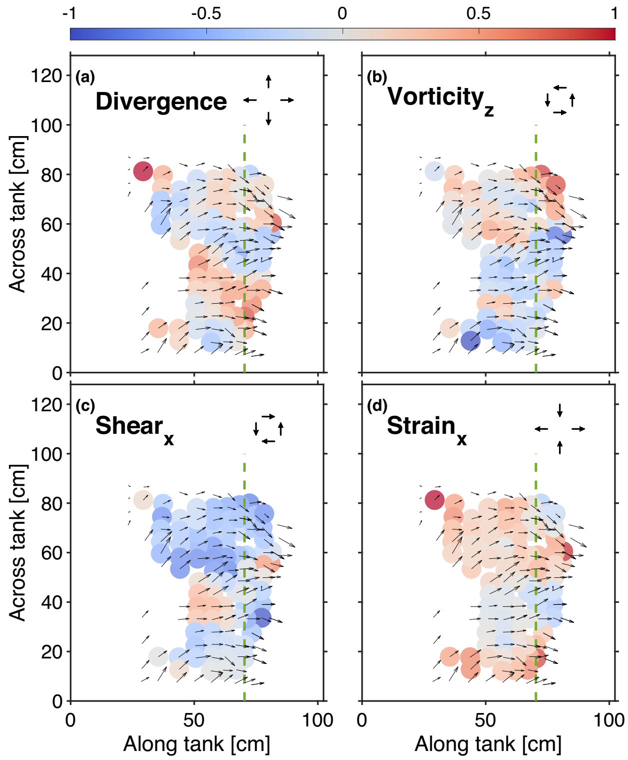

Fig. 7 Panel (**a**) shows instantaneous normalized surface divergence. The dashed green line marks the wave crest. The vector arrow represents the spot's instantaneous velocity. Panel (**b**) shows instantaneous normalized surface vorticity. Panel (**c**) shows the instantaneous normalized streamwise surface shear. Panel (**d**) shows the instantaneous scaled streamwise surface strain. The color scheme indicates normalized gradient magnitude.

the dissipation rate and separation scales. Thus, a $r^{2/3}$ scaling may be expected for the structure function of turbulent velocity measurements made within the surface viscous sublayer.

Kolmogorov's hypothesis of local homogeneity implies that the structure functions depend only on separation, not on position. The unidirectional nature of the flow field (aligned wind and wave direction) and a fetch distance of 10 m makes the flow field unsteady in the streamwise direction, which implies that at a given time, the structure-function in the streamwise direction will be dependent on its location. However, this unidirectionality of the flow field's evolution implies local statistical homogeneity in the spanwise direction (independent of the location where the probability density function (PDF) is calculated). A second-order structure function $D_{ii}(r)$ is defined as the covariance of the fluctuating velocity difference between points separated by a distance r (Pope 2000).

$$D_{ii}(r) = \overline{(u_i'(y) - u_i'(y+r))^2} \tag{14}$$

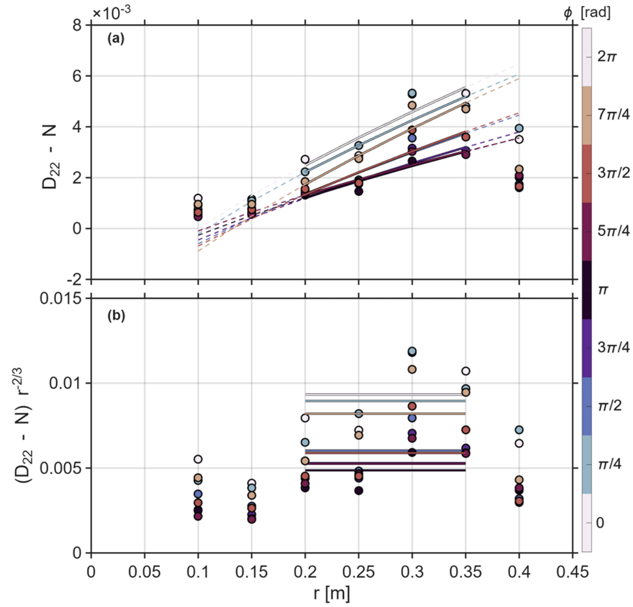

Fig. 8 Panel **a** shows the time and span averaged transverse structure function of streamwise fluctuating velocity (equation 14). The color scheme represents the wave phase. The solid line indicates the least squares fit to the observed $D_{22}(r, \phi)$, based on the relation provided in Eq. 15. Panel **b** shows the compensated structure function. Inertial subrange was identified by inspecting the compensated structure function for the smallest slope and over a sliding window of different sizes. The least squares fitting to infer dissipation rate was performed over the identified window of scales as shown in panel **a**.

Using similarity hypotheses, for homogenous and isotropic conditions and assuming an infinitely long inertial subrange, Kolmogorov 1941 predicted the relationship between dissipation rate (ϵ), r, and D_{11} . The scaling argument presented by Kolmogorov for the three-dimensional homogenous and isotropic case with infinitely long inertial subrane was extended to a two-dimensional system given by Eq. 15 (Lindborg 1999).

$$D_{11}(r) = C_\nu \, \epsilon^{\frac{2}{3}} \, r^{\frac{2}{3}} \tag{15}$$

where, $C_\nu \approx 6.3$ for two-dimensional turbulence (Boffetta and Ecke 2012).

For wind-only cases, horizontal isotropy of the flow field at the surface was investigated by computing the longitudinal and transverse structure functions (D_{11} & D_{22}, respectively) for fluctuating streamwise velocity. A clear region of $r^{2/3}$ scaling was observed in both D_{11} and D_{22}; however, the magnitude of change of the slope within the inertial subrange was observed to be significantly larger for D_{11} relative to D_{22}. This indicate that the flow field for wind-only cases is horizontally anisotropic. This led us to conclude that the transverse and longitudinal structure functions must be examined separately for $r^{2/3}$ scaling, which will indicate the existence of a range of scales where the structure function is independent of viscosity and depends only on ϵ, which in turn is dictated by large scales of the flow field in the transverse and longitudinal directions. For cases with surface gravity waves, we investigated D_{22} for the streamwise fluctuating velocity and D_{11} for the spanwise fluctuating velocity (i.e., our scale vector is oriented in the spanwise direction ($r\hat{y}$)). We did not find any discernible trend in D_{11} of streamwise velocity fluctuation and D_{22} of spanwise velocity fluctuation in the presence of surface gravity waves (in these cases the scale vectors were directed in the spanwise direction ($r\hat{x}$), however, these structure functions are not considered in this study). Span and time-averaged phase conditional observed D_{22} of streamwise velocity fluctuation is shown as filled circles in panel a of Fig. 8.

The observed velocity structure function was averaged in time for every 5° phase bin, which produced a structure function between $r_{\min} < r < r_{\max}$ at 5 cm intervals in the spanwise direction for each phase bin. The time-averaged structure function was then inspected to identify a window within which the compensated structure function had very small slope magnitude (akin to identifying a $k^{-5/3}$ scaling window of wave numbers in spectral techniques). The window size was kept flexible and chosen based on a weight function that selected the largest window with the smallest compensated structure-function slope. The compensated structure function is shown in panel b of Fig. 8. The solid flat line marks the range of scales where the $r^{2/3}$ scaling was observed and the prescribed structure function model given in equation 15 was fitted to the observed time averaged velocity structure using least squares fit for linear model $D(r) = N + Ar^{\frac{2}{3}}$ to obtain the dissipation rate estimates (ϵ), where, $A = C_{\nu}\,\epsilon^{\frac{2}{3}}$ and N is the offset from the measurement noise. The unstructured and sparse nature of the phasogram prohibited the calculation of the integral length scale via autocorrelation. TKE dissipation rate estimates with R^2 value less than 0.5 were rejected for quality control of the model's fit to the observed structure function. Previous studies show the short-scale wind waves typically have a wavelength of roughly 10 cm (Zappa et al. 2008). This motivated selecting the smallest length scale, $r_{min} = 10$ cm, for computing the fluctuating velocity correlation, while the largest scale was restricted to $r_{\max} = L/2$, where L is the length of the thermal grid. The intermediate resolution of the scales was 5 cm, as shown on the horizontal axis of Fig. 15.

3 Results

3.1 Phase-resolved surface velocity and elevation

Figure 9 shows orbital velocity ($\widetilde{u}$) for 2 cm, 4 cm and 6 cm amplitude waves at $U_{10} \approx 5.3$ m/s in panel (a), $U_{10} \approx$ 8.05 m/s in panel(b) and $U_{10} \approx$ 10.2 m/s in panel (c). The phase-conditional averaged wave orbital velocity varies with wave amplitude and shows no appreciable change with an increase in wind speed. In Fig. 9 and all subsequent phase conditional time averaged results (Figs. 10, 11, 13, 14 and 15) are plotted such that wind and waves propagate from left to right and wave's crest are located at 0 and $\pm 2\pi$, while the troughs are located at $\pm\pi$.

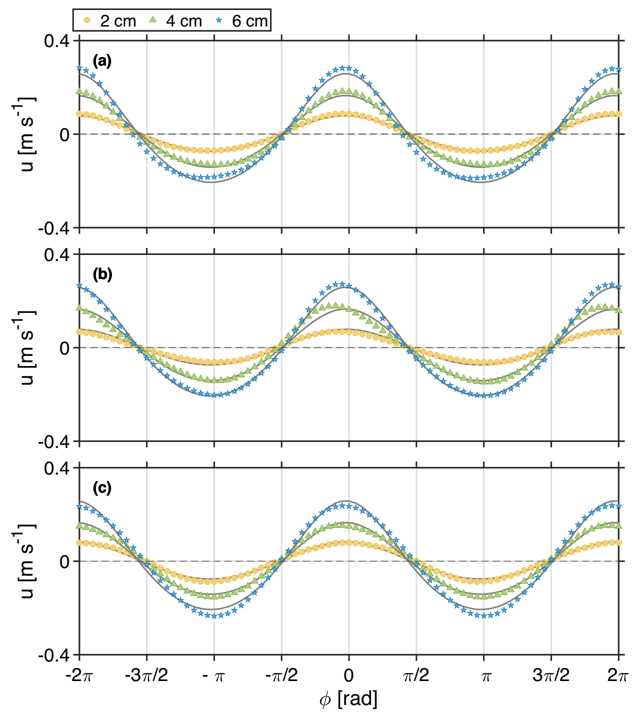

Fig. 9 Panel **a** through **c** are streamwise surface velocity of spots at $U_{10} \approx 5.3$ m/s, 8.05 m/s & 10.2 m/s respectively for wave of 2 cm, 4 cm, and 6 cm amplitude. A representative, scaled wave shape is shown in a thin, gray, solid line. Wind and waves propagate from left to right.

As summarized in Sect. 2.2.5, the theoretical surface elevation for each spot was calculated using a third-order Stokes wave solution. Figure 2 shows the third-order solution of the wave equation is an appropriate choice for a 0.58 Hz wave at all wave amplitudes (2 cm, 4 cm, and 6 cm) analyzed in this work. The theoretical surface elevation of each spot was averaged conditioned to the spot's phase. The phase-conditional averaged theoretical surface elevation and its comparison with independent water surface elevation measurement from the downstream UDM are shown in Fig. 10. Phase information of the independent water surface elevation was calculated via wavelet transform following Laxague et al. (2020). Figure 10 panel-a shows theoretical 1st, 2nd and 3rd order elevation with phase conditional UDM elevation measurements. Panels b through d of Fig. 10 show phase conditional averaged UDM measurements along with their theoretical third-order elevation at reference wind speed $U_{10} \approx 5.3$ m/s, 8.05 m/s & 10.2 m/s srespectively.

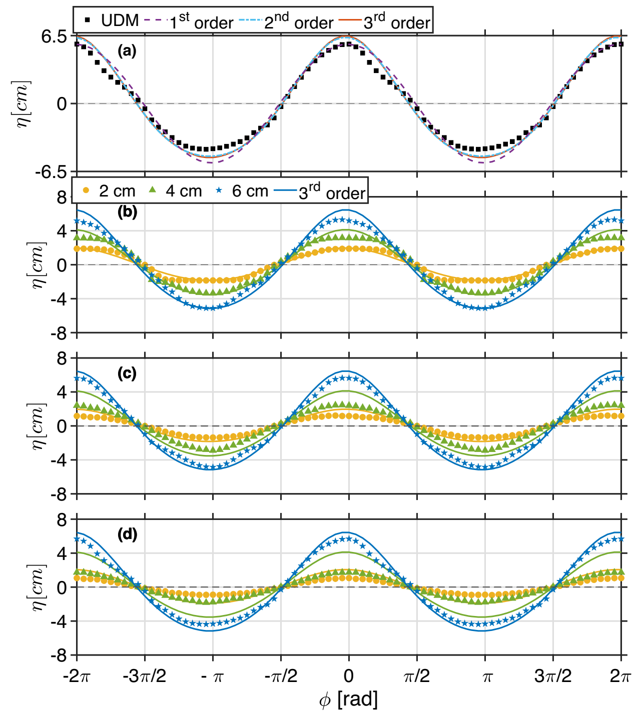

Fig. 10 Panel (**a**) UDM and wave-wire measurements for a 6 cm amplitude wave at 9 Hz fan VFD plotted alongside 1^{st}, 2^{nd} and 3^{rd} order Stokes surface elevation fit. Panels (**b**) through (**d**) are UDM and wave-wire surface elevation at $U_{10} \approx 5.3$ m/s, 8.05 m/s & 10.2 m/s respectively. Line plots represent 3^{rd} order elevation fit of 2, 4, and 6 cm. Wind and waves propagate from left to right.

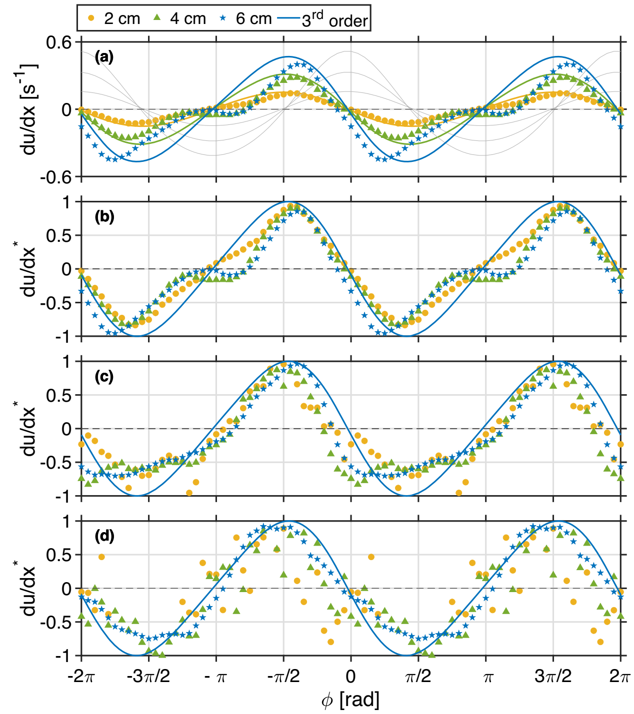

Fig. 11 Panel (**a**) streamwise velocity gradient calculated by projecting surface normal of the local velocity field for 2, 4, and 6 cm wave at 3 Hz fan VFD. Panel (**b**) through (**d**) shows the velocity gradient for 2 cm, 4 cm and 6 cm amplitude waves scaled using maxima of theoretical streamwise velocity gradient at $U_{10} \approx 5.3$ m/s, 8.05 m/s & 10.2 m/s respectively. The solid line represents the normalized theoretical streamwise velocity gradient. Wind and waves propagate from left to right.

3.2 Velocity gradient from unstructured velocity fields

Surface velocity gradient results obtained by projecting the surface normal of a linear fit to the local velocity field, as summarized in section 2.2.6, are presented here. A comparison between the measured streamwise velocity gradient and the expected theoretical third-order velocity gradient using Stokes solution is shown in Fig. 11. Since wind and waves are unidirectional, only the observed streamwise gradient of streamwise velocity ($\frac{\partial u}{\partial x}|_{\text{obs}}$) is shown and compared to its third-order theoretical counterpart ($\frac{\partial u}{\partial x}|_{\text{theory}}$). Panel-a in Fig. 11 shows $\frac{\partial u}{\partial x}|_{\text{obs}}$ as scatter while $\frac{\partial u}{\partial x}|_{\text{theory}}$ as thick colored solid lines for the lowest wind speed of $U_{10} \approx 5.3$ m/s. The representative wave shapes for the 2cm, 4cm, and 6cm waves are plotted in thin gray lines. Panel-b, c, and d in this figure show a direct comparison between $\frac{\partial u}{\partial x}|_{\text{obs}}$ and $\frac{\partial u}{\partial x}|_{\text{theory}}$ at reference wind speed $U_{10} \approx 5.3$ m/s, 8.05 m/s, and 10.2 m/s, respectively. The dimensionless streamwise velocity gradient of streamwise velocity $\frac{\partial u}{\partial x}^*$, is given by equation 16

$$\left.\frac{\partial u}{\partial x}^*\right|_{\text{obs}} = \frac{\frac{\partial u}{\partial x}|_{\text{obs}}}{\max(||\frac{\partial u}{\partial x}|_{\text{theory}}||)} \qquad \left.\frac{\partial u}{\partial x}^*\right|_{\text{theory}} = \frac{\frac{\partial u}{\partial x}|_{\text{theory}}}{\max(||\frac{\partial u}{\partial x}|_{\text{theory}}||)} \tag{16}$$

The scaled velocity gradients shown in panels b, c and d of Fig. 11 show good agreement between $\left.\frac{\partial u}{\partial x}^*\right|_{\text{obs}}$ and $\left.\frac{\partial u}{\partial x}^*\right|_{\text{theory}}$ at all wind speeds. This agreement between the observed and theoretical velocity gradients validates our approach to calculating the unstructured-grid velocity gradient, as summarized in section 2.2.6.

Next, Fig. 12 shows the temporal evolution of normalized streamwise surface wave strain over two wave periods (2×3 seconds). Wind and waves propagate from left to right, and the dashed purple line represents wave troughs, while the dashed green line represents wave crests. The magnitude of strain is normalized by its 99th percentile value. Positive values of strain represent streamwise stretching and spanwise compression, while negative values represent spanwise stretching and streamwise compression. The upwind face shows surface stretching in the streamwise direction, while the downwind face shows compression in the spanwise direction, and the inflection points are the wave nodes [$\pm$ n π (n=odd-troughs n=even-crests)].

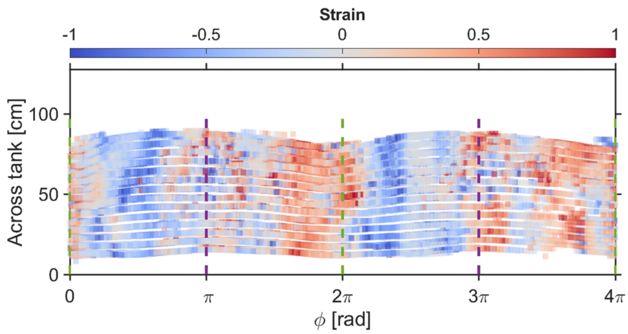

Fig. 12 Instantaneous variation of scaled streamwise surface strain in streamwise direction over two wave periods for a 6 cm amplitude wave at reference wind speed $U_{10} \approx 5.3$ m/s. Green dashed line marks wave crests at 0, 2π, and 4π, while purple dashed line marks wave troughs at π and 2π. Wind and waves propagate from left to right.

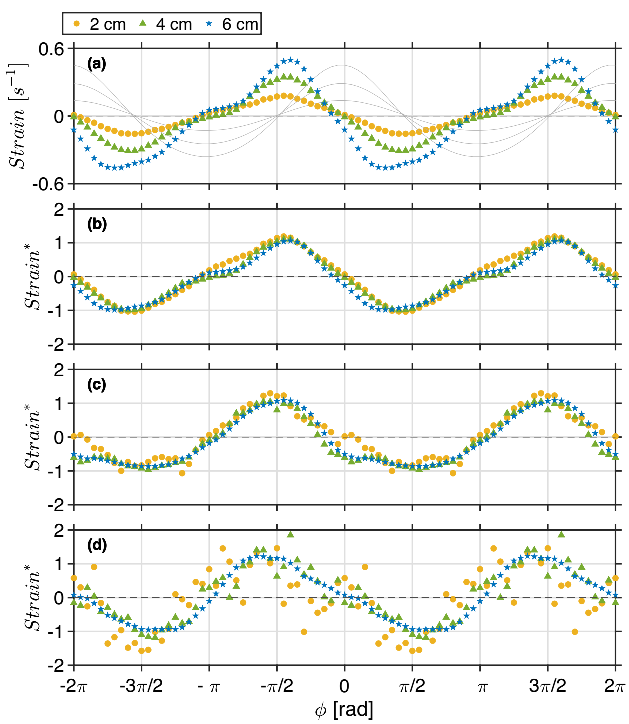

Fig. 13 Panel (**a**) shows the streamwise surface strain as calculated by projecting the surface normal of the local velocity field for 2, 4, and 6 cm waves at 3 Hz fan VFD. Panel (**b**) through (**d**) shows streamwise surface strain for 2 cm, 4 cm and 6 cm amplitude waves scaled using maxima of theoretical streamwise velocity gradient at reference wind speed of $U_{10} \approx 5.3$ m/s, 8.05 m/s & 10.2 m/s respectively. Wind and waves propagate from left to right.

Figure 13 shows wave phase conditional ensemble-averaged surface wave strain on the entire run. Panel a in Fig. 13 shows wave phase conditional ensemble averaged strain over the entire run at reference wind speed $U_{10} \approx 5.3$ m/s for 2 cm, 4 cm, and 6 cm wave amplitude. The solid gray line in this plot represents a scaled wave shape. The magnitude of surface strain shows a strong correlation with wave amplitude. As the instantaneous surface strain plot in Fig. 12 suggests, the surface wave strain is negative on the downwind face (surface gravity wave's leading front). Panel-b, c, and d of Fig. 13 show scaled surface strain at increasing reference wind speeds $U_{10} \approx 5.3$ m/s, 8.05 m/s and 10.2 m/s, respectively. The surface strain was scaled by $\max(||\frac{\partial u}{\partial x}|_{\text{theory}}||)$ since, for a unidirectional wave, the most significant contribution to irrotational wave strain will come from the streamwise gradient. Further, an examination of Fig. 13 shows that the observed surface strain closely agrees with $\frac{\partial u}{\partial x}|_{\text{theory}}$. A relative comparison of surface strain at $U_{10} \approx 5.3$ m/s (panel-b Fig. 13) and $U_{10} \approx 10.2$ m/s (panel-d Fig. 13) highlights the effect of increased wind stress on wave strain. At the highest wind speed (cases for which the wind stress is particularly high on the upwind face), surface strain varies strongly on the upwind face and weakly on the downwind face. Furthermore, the phase of maximum strain moves windward to the upwind face of the wave.

3.3 Phase conditional averaged surface TKE and dissipation rate

Figure 14 shows the ensemble phase conditional time-averaged surface TKE response to the mechanically generated wave's shape. Kinematic constraints of the interface suppress vertical velocity fluctuations at the surface (Guo and Shen 2010), and the total TKE (q^2) is defined as the sum of directional streamwise and spanwise TKE (q_x^2 and q_y^2). Panels a, c, and e in Fig. 14 show q_x^2, and panels b, d, and f show q_y^2 where wind speed increases down the row. The grid spacing ($\sim$ 5 cm) prevents the isolation of short wind waves; hence, these motions are erroneously included in the surface TKE measurements of this study. At all wind speeds, the ensemble-phase-conditional-averaged TKE exhibits apparent wind-speed- and phase-dependent behavior. Across all wind speeds, TKE is observed to be greatest at the crests of the dominant waves, a finding consistent with other experimental studies (Jiang and Street 1991; Rashidi et al. 1992; Thais and Magnaudet 1996). However, spanwise TKE appears independent of the wave phase, with no substantial peaks at any wind velocity.

At low wind speeds, the airflow streamlines follow the wave's waveform and, on the leeward side of the wave, impart stress and drive the mean surface current (Kawai 1982). The observed behavior of streamwise TKE for $U_{10} \approx 8.05$ m/s & 10.2 m/s is in qualitative agreement with the values reported in Savelyev (2020), and both results are of similar orders in magnitude. However, the point of departure for streamwise TKE agreement from those reported in Savelyev (2020) is at $U_{10} \approx 8.05$ m/s, which shows a secondary peak at wave troughs. Spanwise TKE reported in this study shows no discernible response to wave shape and increases with

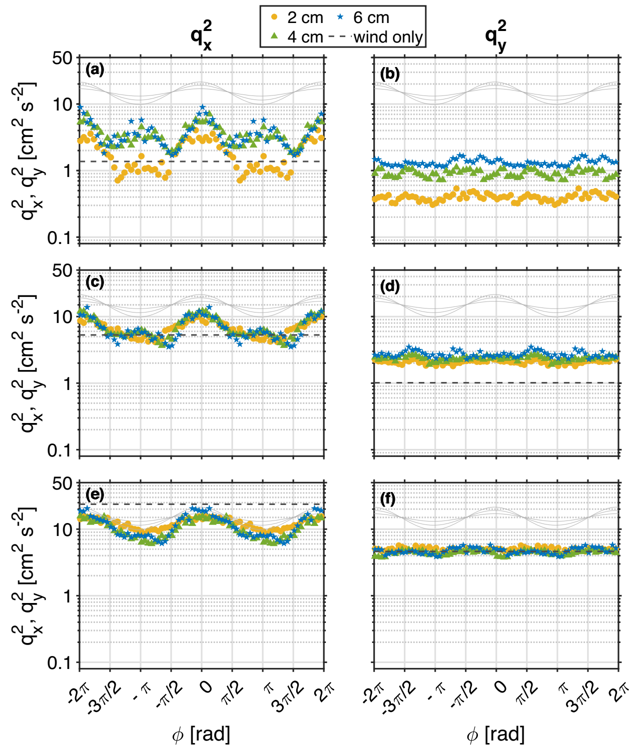

Fig. 14 Panels (**a**), (**c**), and (**e**) show streamwise surface TKE, while the panels (**b**), (**d**), and (**f**) show spanwise TKE. Reference wind velocity increases down the row $U_{10} \approx 5.3$ m/s, 8.05 m/s & 10.2 m/s respectively for waves of amplitude 2 cm, 4 cm, and 6 cm. A representative, scaled wave shape is shown in a thin, gray, solid line. Wind and waves propagate from left to right.

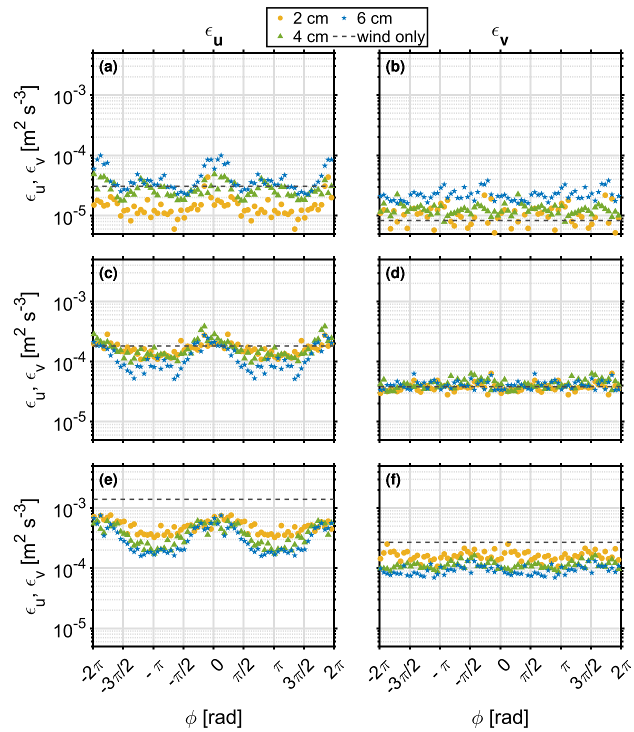

Fig. 15 Panels (**a**), (**c**), and (**e**) show the streamwise surface TKE dissipation rate, while the panels (**b**), (**d**), and (**f**) show the tank TKE dissipation rate. Reference wind velocity increases down the row $U_{10} \approx 5.3$ m/s, 8.05 m/s & 10.2 m/s respectively for waves of amplitude 2 cm, 4 cm, and 6 cm. A representative, scaled wave shape is shown in a thin, gray, solid line. Wind and waves propagate from left to right.

increasing wind speed. This contrasts with the findings of Savelyev (2020), who reported a peak in the spanwise TKE magnitude at the wave crest across all wind speeds.

The dashed line in Fig. 14 represents phase conditional, space and time-averaged directional TKE for wind-only conditions. This wind-only directional TKE magnitude provides a reference for identifying the mean and phase-varying impact of surface gravity waves. At the lowest wind speed, the TKE at all wave amplitudes exceeds the wind-only case TKE; however, at $U_{10} \approx 8.05$ m/s, the wind-only TKE magnitude is exceeded only at regions close to the wave crest, and at 9 Hz wind fan VFD, only the TKE magnitude at the wave crest matches the wind-only case magnitude. A similar trend is observed for spanwise TKE where the relative magnitude between the wave with wind and wind-only cases decrease between $U_{10} \approx 5.3$ m/s to $U_{10} \approx 8.05$ m/s before the wind only TKE attains magnitude similar to the magnitude of wind and wave case runs at $U_{10} \approx 10.2$ m/s. The decrease in the relative magnitude between TKE in the wave case and TKE in the wind-only case with increasing wind speed aligns with the observations made by Savelyev (2020) and was identified to be the result of sheltering.

Figure 15 shows streamwise and spanwise TKE dissipation rate inferred using D_{22} for streamwise velocity fluctuation and D_{11} for spanwise velocity fluctuation. Streamwise TKE dissipation rate (ϵ_u) is shown in panels a, c, and e while spanwise TKE dissipation rate (ϵ_v) is shown in panels b, d, and f, with reference wind speed increasing down the rows $U_{10} \approx 5.3$ m/s, 8.05 m/s and 10.2 m/s respectively. Spanwise turbulence dissipation rate ϵ_v does not show any dependence on long wave phase. At all wind speeds, streamwise TKE dissipation rate ϵ_u exhibits absolute maxima at the wave crests for all wind speeds. This follows the behavior observed for the TKE. The phase dependence of ϵ aligns with the structure-function dependence within the identified inertial subrange on the wave phase shown in Fig. 8, where steeper slopes (higher ϵ) are observed at wave crests, while milder slopes at wave troughs (lower ϵ). At low wind speeds, there is substantial separation of mean ϵ_v relative to wind-only cases; this difference gets progressively smaller for increasing wind speed.

3.4 Effect of vortex force

The mean flow motion of wave current interaction can be approximated by applying an appropriate higher-order correction term. The correction term (vortex force) transfers streamwise momentum in the spanwise direction and arises from the first-order straining of the surface vertical vorticity vector due to irrotational surface waves. The vortex force correction term provides necessary momentum to perturb vertical stability, which could lead to the generation of spanwise-oriented counter-rotating eddies (Leibovich 1977, 1980). The instantaneous second-order effect of vortex force is overshadowed by the first-order direct straining due to the wave's orbital motion. However, the cumulative effect of the second-order vortex force is identified as a key parameter that provides the necessary spanwise momentum at the surface to initiate and maintain the vertical counter-rotating eddy pairs (Noh et al. 2004; Sullivan et al. 2007). The surface signature of these eddies is downwelling regions where cooler water converges (convergence zone) and upwelling regions where relatively warmer water is transported from below the surface by the vertical eddy (divergence zone). In a grayscale infrared image of a surface, the convergence and divergence zones show up as regions of low (dark) and high (bright) intensity, respectively. In this section, we quantitatively investigate the effect of vortex force on the location and size of vertical eddies by simultaneously tracking the locations and diameters of surface convergence and divergence zones using grayscale thermal images and the spatial distribution of the vortex force field.

Visual inspection of the infrared images showed sustained dark convergence and bright divergence zones across a handful of runs in cases with a 6 cm wave amplitude (or steepest slope), high wind velocity ($U_{10} > 8$ m/s), and warmer water. Table 2 entries list the run and their experimental parameters for cases that showed prominent surface convergence and divergence zones. The surface vorticity field was first calculated from the active thermal markers as summarized in section 2.2.6. Following this, the active thermal markers we filtered out of the grayscale image (say $I_{\text{background}}$) using morphological operation (in context to the nomenclature used in section 2.2.2, the filtered image is given by ($I_{\text{background}} = I_{\text{grayscale}} - I_1$)). The columns of the background image were arranged in a phasogram according to the gravity wave's phase. Stacking of the images in the phasogram was initiated when the long-wave phase(ϕ) of $\pi/8$ was close to the right edge of the frame. This ensured continuity in the allocation of filtered images and vortex force in the phasogram at $\phi = 0$ and 4π (i.e., for two wave periods (167 frames)). The resulting phasogram image stack was averaged in time and is shown in the top-left panel in Fig. 16, showing sustained convergence and divergence zones across two wave periods. The plot in the top-right panel of Fig. 16 shows the polynomial fit to the phase-averaged grayscale intensity fluctuations. The dashed line marks the location of the minima (convergence zone) and the maxima (divergence zone) in the flow field over two wave periods. The location of convergence and divergence zones was identified using an image intensity polynomial, along with the individual eddy diameter, which was calculated at every two wave period intervals (167 frames) for four runs listed in Table 2.

The Craik-Lebovich (CL) equation for Langmuir circulation in the Eulerian frame of reference for constant eddy viscosity is given by equation 17 (Leibovich 1980).

$$\frac{\partial \vec{u}}{\partial t} + \vec{u} \cdot \nabla \vec{u} + \nabla (P + \vec{u} \cdot \vec{u^s}) = \vec{u^s} \times (\nabla \times \vec{u}) + \nu \nabla^2 \vec{u} \tag{17}$$

where $\vec{u^s}$ is the wave averaged Stokes drift velocity given by equation 18 (Mascheck 1979)

$$\vec{u^s} = \frac{\omega k a^2 \cosh(2k(z+d))}{2\sinh^2(kd)} \tag{18}$$

The first term on the right in equation 17 is the vortex force in the Eulerian frame of reference. The long-wave phase-conditioned spanwise distribution of vortex force was arranged in a phasogram and averaged over the same two wave-period intervals as the filtered images. The two-dimensional unstructured grid time-averaged vortex force array was uniformly gridded using linear interpolation, and its contour distribution is shown in the bottom left panel of Fig. 16. The smallest resolvable scale of vortex force depends on the smallest resolvable scale of vorticity. The smallest resolvable scale of the velocity gradient-derived quantities depends on the spacing of the unstructured grid and on our velocity gradient calculation methodology (detailed in Sect. 2.2.6), which requires at least three points for surface vorticity estimates. The smallest resolvable scale of freely evolving unstructured grid vortex force (or vorticity) measurement thus varies, depending on space and time, from an initial scale of 11 cm. The wave-phase-conditioned vortex-force distribution was then divided into a phase window of width $\pi/4$. The location of the bin edges is shown as a thin gray solid rectangular box overlaying the vortex force contour map in the bottom left panel of Fig. 16. The width of the first and last windows is reduced to $\pi/8$ for maintaining continuity of phase windows at long wave phase of $\phi = 0$ and 4π. In further analysis, the first and last phase windows were combined into a single window. Vortex force within each window was averaged along phase, and the location of the convergence and divergence zones was identified by zero crossing of the piecewise linear fit to the windowed phase average distribution. Zero crossing with a negative slope of the fit marks a convergence zone, while a positively sloped zero crossing marks the location of divergence zones. The location of the zero crossing within each phase window is shown as a black dashed line spanning the width of the window. All the identified zero crossings within every phase bin were

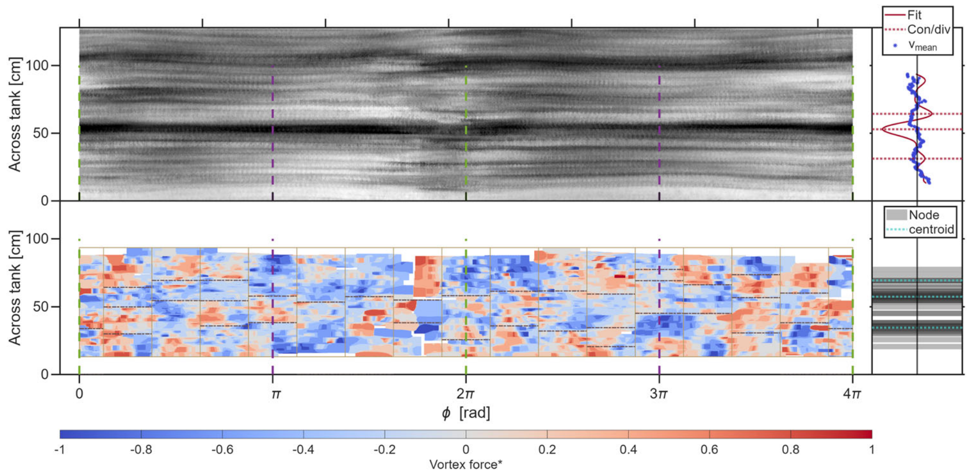

Fig. 16 Top left panel shows phase-conditional averaged grayscale thermal background intensity ($I_{grayscale}$). The top-right panel shows the phase-averaged grayscale 25th- order polynomial fit (solid line). The dashed markers are the locations of the fit polynomial's maxima (divergence zones) and minima (convergence zones). The blue $'*'$ shows the phase averaged mean spanwise velocity distribution over two wave period considered. The bottom-left panel shows a contour plot of the Eulerian distribution of vortex force, scaled by its 99th percentile. The overlaying solid gray rectangular box indicates an individual investigation window. The dashed black lines within the investigation window mark zero crossing of the piecewise linear fit to the phase-averaged vortex force within the investigation window. The bottom-right plot shows a collection of zero crossings from all investigation windows, shaded as regions. Using a distance-based clustering algorithm (K-means), vortex force node clusters were identified. The centroid of these zero-crossing clusters is chosen as an effective vortex force node. Wind and waves propagate from left to right.

Table 2 Run number along with their experimental parameters and water temperature used in analyzing the effect of vortex force on the arrangement of thermal structures on the interface.

Run	a_{fit}^{3rd} [cm]	σ_w [Hz]	Fan [Hz]	U_{10} [m/s]	u_{air}^* [m/s]	T_w [°c]	T_a [°c]
44	6.50	0.58	9	10.4	0.300	32.8	31.51
45	6.42	0.58	6	8.2	0.177	32.8	31.89
49	6.50	0.58	9	10.3	0.300	31.8	31.00
50	6.47	0.58	6	8.2	0.177	31.6	30.43

collected and clustered using the k-means algorithm. Clustering of all identified nodes from the phase bin was motivated by the objective of the intended analysis, wherein we compared the location and diameter of sustained convergence and divergence zones obtained from the grayscale image to the predictions obtained from the cumulative effect of vortex force over the same two wave periods. The centroid of the clustered nodes was selected as a sustained convergence and divergence location identified using vortex force distribution over two wave periods. The bottom-right panel of Fig. 16 provides a qualitative visualization of the clustering process. A broad shaded region of partial transparency is plotted at the node location collected from every phase window. The darker region marks the location of high node density. The overlaid dotted line marks the location identified as the centroid of the clustered node locations obtained from the k-means algorithm. The predicted node location and eddy diameter were obtained at every two wave period interval (167 frames) for four runs listed in Table 2.

Before making a direct comparison of eddy diameters calculated from a grayscale image with predictions from vortex force, the accuracy of individual measurements and the smallest comparable scales of eddy diameter need to be addressed. The high-resolution grayscale image can detect eddy diameter accurately down to $O \sim$ mm, while vortex force nodes are dependent on the smallest resolved vorticity scale, which is accurate down to $O \sim 11$ cm. The RMSE between the identified zones of convergence/divergence in the grayscale images-over two wave periods-and the predicted locations from vortex force measurements, across all four runs, ranged from 8 cm to 10 cm. This motivated excluding grayscale eddy diameters smaller than 11 cm, as well as the corresponding predictions from the vortex force measurements. Figure 17 shows the mean (solid line) of a 1:1 comparison for every 10 measurements between the eddy diameter as observed from the image intensity fit and the eddy diameter predictions derived from the sustained vortex force zero crossing nodes. The shaded region shows the 95% confidence interval bounds for the mean. The

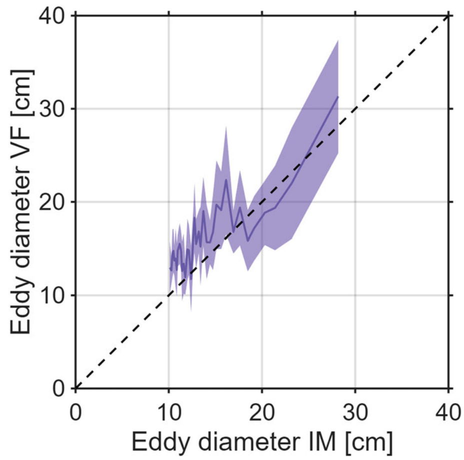

Fig. 17 1:1 comparison of eddy diameter obtained from spatial distribution of vortex force and image intensity. The shaded region indicates the 95% confidence interval bound of the mean value.

results show agreement between the observed grayscale eddy diameter and the predicted diameters from vortex-force measurements.

4 Discussion

4.1 TKE and dissipation rate

Our measured surface velocities comprise the contributions from mean flow, the orbital motions of the dominant mechanically generated waves, the orbital motions of the high-frequency wind-generated waves, and the turbulent motions. The TKE magnitude reported in this work is isolated from the gravity wave orbital motion and mean current; however, , the high-frequency short wind waves' orbital motions are erroneously included within the values reported in Fig. 14. The gravity-capillary and short gravity waves which may impact are measurement must be large enough to be resolved by our TMV measurement but small enough to evade removal via wave phase-conditional averaging. The small end of this range is constrained by the ≈1 cm TMV spot diameter and the assumption that a wave is not properly resolved unless it is sufficiently larger than the measurement region; the large end of this range is constrained by the extremely fetch-limited wind-wave growth conditions in SUSTAIN. Based on laser-induced fluorescence measurements of water surface elevation (Tenhaus et al. 2024) , we estimate the peak wavelength among the wind-generated waves to be ≈10 cm at our fetch of 10 m. This indicates that contamination of the turbulent velocity signal is originating from waves in a very narrow spectral bandwidth (5-10 cm wavelengths). Based on small-amplitude gravity-capillary wave theory, we estimate the size of this contamination to be no more than the same order of magnitude as turbulent intensities. However, the structure-function analysis provides evidence that the fluctuating velocity signal has a dominant turbulent signature from large-scale motion. Reduction of the streamwise TKE magnitude shown in (panel (a) of Fig. 14) at the lowest wind speed relative to the wind-only case could be speculated to be a result of the suppression of high-frequency waves due to the presence of low-frequency long waves. Previous experimental investigations show that suppression of high-frequency wind waves is preferentially located at the wave trough and is independent of low-frequency paddle wave breaking (Shabani et al. 2022). Donelan et al. (1987) explored the effect of the rate of wind input for mild and steep wave slope cases and observed that the low frequency and less steep waves suppress the wind input to rates below wind-only cases. Relatively higher sloped waves enhance the wind input rate above wind-only cases (see their Fig. 5).

As mentioned above, we are not able to remove the orbital motions associated with very short wind waves, so those motions are erroneously included within the turbulence energy shown in Fig. 14, however, the range of scales used for estimation of dissipation rate magnitude shown in Fig. 15 is larger than the wavelength of a typical short wind wave. Further, for our unidirectional flow field, we compute the structure function with the scale-separation vector oriented in the spanwise ($r\hat{y}$) direction. Streamwise propagating, intermittent short wind waves will have an irrotational velocity component in the streamwise direction, while our scale separation vector ($r\hat{y}$) is oriented perpendicular to the dominant streamwise flow field. This would imply that even in the presence of a wide crested unresolved short wind wave, which contributes to our fluctuating velocity magnitude, its structure function (which is the difference of the fluctuating velocity field separated by $r\hat{y}$) will remove those irrotational contributions from short wind waves. Further, the implementation of an adjustable window fit, as demonstrated in Fig. 8, shows the $r^{2/3}$ scaling exists at scales larger than the smallest scale used in the computation of the structure function. Using a 10cm lower-bound separation ensures that the structure-function–based ϵ estimates exclude the energetic scales of short wind waves. The surface TKE dissipation rate estimates of this study show qualitative agreement with previous estimates of breaking wave conditions close to the surface, at $O(\sim 60\text{ cm})$ (Terray et al. 1996; Soloviev and Lukas 2003). Further, Gemmrich et. al. [2003] (Gemmrich and Farmer 2004) observed a "significant" increase of average dissipation rate above the mean water level and nearly constant values in the trough region for breaking and non-breaking waves. The average increase in TKE dissipation rate in the presence of surface waves and a higher than average dissipation rate close to the wave crest agrees with the result of this study and with the scaling dependent on energy flux from wind to waves and significant wave height proposed by

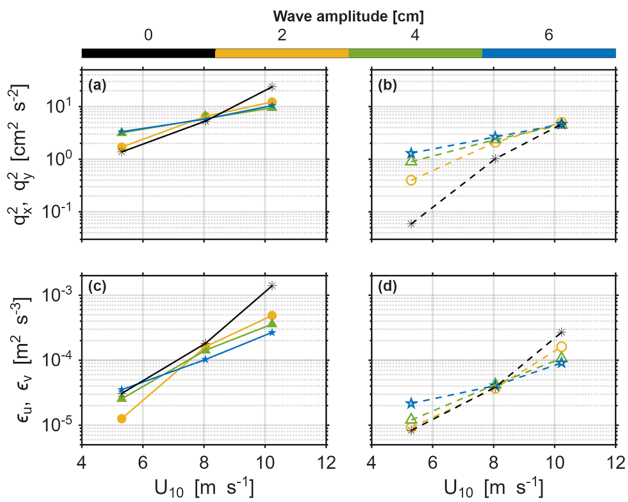

Fig. 18 Ensemble condition and phase averaged surface (**a**) streamwise TKE (q_x^2) (**b**) spanwise TKE (q_y^2) (**c**) streamwise TKE dissipation rate (ϵ_x), and **d** spanwise TKE dissipation rate (ϵ_y) for 0.58 Hz wave and wind only condition (wave amplitude = 0) at $U_{10} \approx 5.3$ m/s, 8.05 m/s & 10.2 m/s.

Terray et. al. [1996] (Terray et al. 1996). Siddiqui et.al. [2010] (Siddiqui and Loewen 2010) reported observations 1 mm below the surface, which showed significantly increased TKE dissipation rates at the wave crest for cases with microscale wave breaking. The increase of streamwise dissipation rate near the interface shows qualitative agreement with the result of this work reported in Fig. 15. Streamwise TKE dissipation rate ϵ_u at the wave crest is higher than the rest of the wave phase for every wave amplitude at all wind speeds.

At the lowest wind speed ($U_{10} \approx 5.3$m/s), no wave breaking was observed, while at moderate wind speed ($U_{10} \approx 8.5$m/s), sparsely distributed small length breakers were observed. In contrast, at the highest wind speed, significant breaker density was observed even for the wind-only cases. Panels (a) and (b) of Fig. 18 show ensemble condition-averaged streamwise and spanwise TKE as a function of wave amplitude (or slope) and wind speed. Consistent with previous measurements, at low wind speed, a monotonic increase of streamwise TKE magnitude is observed with increasing wave amplitude. While at the highest wind speed, increasing wave amplitude reduces streamwise TKE relative to wind-only TKE magnitudes. (Savelyev et al. 2020). Panel (b) of aure 18 shows a similar monotonic increase in spanwise TKE magnitudes at the lowest wind speeds. In contrast, at the highest wind speed, the spanwise TKE magnitude is independent of wave amplitude and asymptotes to the same constant value in the absence and presence of surface gravity waves. Savelyev et al. [2020] proposed two primary reasons for the observed trend of streamwise and spanwise surface TKE. First, the vortex force enhances momentum transfer primarily in the spanwise direction by generating vertical, coherent, counter-rotating structures at low wind speeds and increasing wave amplitude (or steepness). Second, at higher wind speeds, airflow separation shelters the surface, reducing turbulence despite the greater momentum flux.

Panels (c) and (d) of Fig. 18 show the ensemble condition-averaged streamwise ϵ_u and spanwise ϵ_v TKE dissipation rate. At all wind speeds, the wind-only streamwise TKE magnitude remains higher than in cases with surface gravity waves. At the lowest wind speed, a significant reduction in TKE dissipation rate is observed for the lowest wave amplitude case, where, with increasing wave amplitude, the dissipation rate increases to a magnitude comparable to the wind-only case. Whereas, spanwise TKE dissipation rate shows an amplification of spanwise TKE dissipation rates with the addition of surface gravity wave, and further increases with increasing wave amplitude. The TKE dissipation rates are governed by large-scale structures, and a decrease in the streamwise TKE dissipation rate, while a simultaneous increase in the spanwise TKE dissipation rate, indicates that the addition of surface gravity waves facilitates the transfer of streamwise turbulent energy in the spanwise direction. Further, at low wind speed in the absence of sheltering, increasing wave amplitude amplifies wave strain, modulating surface turbulent structures and increasing the surface area for wind input. The combined effect of the above phenomenon can be speculated to increase the shearing effect on surface turbulent structures and to enhance the dissipation rate with increasing wave amplitude at the lowest wind speed (Xiao et al. 2009; Baker et al. 2023). At moderate wind speed, an inflection point is observed in both streamwise and spanwise TKE dissipation rates. At the highest wind speed, strong evidence of wind-wave sheltering is observed, where, with increasing wave amplitude, the dissipation rate decreases for both the streamwise and spanwise velocities.

4.2 Influence of vortex force on surface convergence and divergence zones

Craik-Leibovich (CL) equations (Leibovich and Paolucci 1980; Leibovich and Radhakrishnan 1977; Leibovich 1977) are the appropriate approximation to the full Navier-Stokes wave current interaction equation (Leibovich 1980) for a small amplitude irrotational wave field. The averaged CL equation requires a correction for rotational current to the wave field. To quantify the correction, it is necessary to obtain the vorticity vector associated with wave activity at the surface. In the final averaged CL equation (equation 17), the correction term (Vortex force) facilitates the interaction of current with waves via Stokes drift (equation 18) due to an irrotational, second-order effect of the wave-field. Bottom left panel of Fig. 16 shows a surface contour map of the vortex force term over two wave periods. The cumulative effect of the second-order Stokes drift grows over time (Teixeira and Belcher 2002), suggesting that while the magnitude of the vortex force is small, it plays a significant role in the organization and size of the vertical counter-rotating eddies.

The surface vorticity vector is stretched and compressed by first-order straining due to wave action. This aligns with the distinct distribution of vortex force and its zero crossing nodes across different wave phase windows shown in the bottom left panel of Fig. 16. Variation in the vorticity vector across different wave phases prompted the windowing of the vortex force contour map to identify the predicted spanwise location of phase-varying vortex force nodes. Figure 17 shows a one-to-one comparison between the eddy diameter observed from the grayscale infrared images and predictions from the vortex force field (described in section 3.4). The agreement of result shown in Fig. 17 indicates that the sustained distribution of surface vortex force significantly influences both the size and the surface organization of vertical counter-rotating eddies.

The contour plot of the time average phase conditioned spanwise Eulerian vortex force distribution can also be used to interpret the vertical vorticity field at the interface, as the vortex force is preferentially oriented spanwise. A region of positive vortex force corresponds to negative vorticity (vorticity vector directed along the negative z-direction) and vice versa for regions of negative vortex force at a two-dimensional interface. The areas of highly localized and fast-rotating structures are located at and around wave crests. This increase in vertical vortex structure at the wave crest(dashed green line) is a result of increased wave breaking at the wave crest or increased spanwise wind stress perturbations relative to the wave trough. These individual vortices interact and are either sheared and cascaded into local turbulence statistics or absorbed by stronger vortices of the same sign (Mcwilliams 1984; Tabeling 2002).

At the highest wind speeds, velocity gradient measurements reported in this work exhibit significant noise (panel (d) of Figs. 11 and 13 shows increased noise level at low wave amplitude, whereas a relatively smooth curve is observed at the highest wave amplitude. However, the velocity, TKE, and TKE dissipation rate do not exhibit the same level of noise at the highest wind speeds and low-amplitude cases, where the wind input is stronger than in higher-amplitude cases. As a result, fewer points will be available within the nearest-neighbor region, resulting in noisy estimates for high wind speed and low wave amplitude. However, at the highest wind speed, the amount of wind input decreases with increasing wave amplitude due to sheltering. Thus, at high wind speeds and high wave amplitudes, the cloud density of thermal markers within the nearest neighboring area will be higher for higher amplitude waves than it will be for lower amplitude cases. To test this hypothesis, we conducted a sensitivity study to determine whether the thermal marking technique itself is susceptible to increased noise at high wind speeds, or whether this is a result of our use of a constant-radius nearest-neighbor region for calculating the velocity gradient across all wind speeds, which, due to sheltering, leads to a noisy signal at low wave amplitude whereas we see a well behaved distribution at highest wave amplitude for the highest wind cases. The sensitivity analysis was conducted for two runs with U_{10} of 8.05 m/s and 10.2 m/s, respectively, and a matching wave amplitude of 2 cm. Four different nearest-neighbor radii, 7 cm, 13 cm, 20 cm, and 25 cm, were tested for both runs. The average RMSE was calculated relative to the theoretical weakly nonlinear third-order estimates for each spot. At U_{10} of 8.05 m/s, the smallest RMSE was observed for a 13 cm radius, while at the highest wind speed, the smallest RMSE was observed for a 25 cm radius. This further indicates a strong sheltering effect at high wind speeds and high wave amplitudes.

A sensitivity analysis showed that the intensity and velocity-based quality control measures discussed in section 2.2.4 reduced the RMSE between the theoretical streamwise velocity gradient and its observed counterpart from $\sim$ 1.1 [s^{-1}] when no velocimetric quality control was implemented, to $\sim$ 0.5 [s^{-1}] when all three velocimetric quality control was turned on. The representative-run sensitivity analysis of intensity and velocity-based quality control measures reflects computational limitations but does not affect the generality or validity of the conclusions.

5 Conclusion

This work presents an extension of TMV for the retrieval of surface velocity gradients and TKE dissipation rates for an undulating wind-ruffled surface. The objective of the experimental work was to obtain spatial measurements of the surface velocity field. The water surface's opacity to longwave infrared radiation was used to mark thermal tracers non-intrusively. The thermal tracers were tracked using an infrared camera, producing a spatial velocity field. The surface velocity field was used to estimate the theoretical third-order surface elevation using the third-order Stokes solution of the wave equation. A comparison between velocity-derived and independent surface elevation using UDM is presented in Fig. 10 and shows good agreement. The estimated surface elevation was used to correct for the disparity caused by the difference in elevation between the calibration and measurement planes. Thermal markers on the interface are steered by the velocity gradient near the fluid parcel. The nearest-neighbor approach was used to calculate the first-order velocity gradient on the unstructured grid. A local linear nearest-neighbor velocity fit projection was used to calculate the velocity gradient at the interface. The first-order streamwise velocity gradient showed good agreement with the weakly nonlinear theoretical expectation. Although no independent spatial surface-gradient instrument exists and no experimental measurements are reported in the literature, the phase-consistent, repeatable du/dx behavior across ensembles, and its agreement with theoretical expectations, support the robustness of the measurement.. Using observed spatial surface velocity gradients, we report the wave phase, conditional time, and the spanwise-averaged surface wave strain at increasing wind speeds. The surface strain conditioned by the gravity-scale long-wave phase indicates that the primary contribution comes from the streamwise gradient of the streamwise velocity.

The spatial velocity field at the wavy surface was then used to calculate the surface TKE response to propagating surface gravity waves. A structure function-based approach was then used to calculate the TKE dissipation rate of the surface flow field as a function of long wave phase. The TKE response to wave shape showed qualitative agreement with previous measurements, where surface TKE peaked at the wave crest. The magnitude of TKE reported in this study is within an order of magnitude of previous active thermal marking measurement (Savelyev et al. 2020). However, we note that the short wind waves were erroneously included in our TKE magnitude. The contribution of irrotational short wind waves to the computed structure function was avoided by the selection of scales larger than the previously reported observed wavelength of short wind waves. Similar to observations by Savelyev [2020] (Savelyev et al. 2020) of TKE response to wind speed and wave amplitude (or slope), at low wind speeds, our measurements show that the streamwise TKE is positively correlated with wave amplitude, while at high wind speeds, surface TKE shows a negative correlation with wave amplitude. The streamwise TKE dissipation rate shows a similar positive correlation with wave amplitude at low wind speed, whereas a negative correlation at higher wind speed. Furthermore, spanwise TKE shows a similar positive correlation with wave amplitude at low wind speeds, but asymptotes to a constant value at the highest wind speed for all wave amplitudes. Spanwise TKE dissipation rate shows an increase in magnitude relative to the wind-only case at the lowest wind speed with increasing wave amplitude. However, an inflection point is observed at mid wind speed, while at the highest wind speed, the spanwise TKE dissipation rate shows a negative correlation, increasing in magnitude.

Using surface vorticity and second-order surface Stokes drift velocity, we calculated the Eulerian vortex force distribution at the surface. A one-to-one comparison of the eddy diameter observed in a grayscale infrared image and the predicted diameter from the vortex force surface distribution showed good agreement. This agreement indicates that surface vortex force distribution strongly influences the organization and size of vertical counter-rotating eddies. Thermal marking velocimetry described in this work did not come without its limitations, specifically, the thermal grid pattern employed for this work restricts isolation of short wind waves. Further, the measurement plane temperature also influenced the magnitude of noise in the measurements: warm water led to a significant number of false detections, while cooler measurement plane temperatures resulted in short-lived spots. In this work, we demonstrate that Thermal marking velocimetry, despite its limitations, can measure velocity, simultaneous horizontal spatial gradients, and turbulence statistics at the wind-ruffled, undulating air-water interface.

Author Contributions SS—Data curation, formal analysis, investigation, methodology, validation, visualization, writing-original draft, and editing. NL—Conceptualization, funding acquisition, investigation, methodology, validation, project administration, resources, writing-original draft, and editing. IS—Data curation, funding acquisition, investigation, methodology, project administration, resources, writing-original draft, and editing. CZ—Funding acquisition, investigation, project administration, resources, writing-original draft, and editing.

Data Availability The codes and data required to reproduce the results shown here may be obtained at the DOI: https://doi.org/10.5281/zenodo.19076672.

Declarations

Competing interests The authors declare no competing interests.

References

Baker CM, Moulton M, Chickadel CC, Nuss ES, Palmsten ML, Brodie KL (2023) Two-dimensional inverse energy cascade in a laboratory surf zone for varying wave directional spread. Phys Fluids 35(12):125140. https://doi.org/10.1063/5.0169895

Banner ML, Peirson WL (1998) Tangential stress beneath wind-driven air-water interfaces. J Fluid Mech 364:115–145

Batchelor GK (1969) Computation of the energy spectrum in homogeneous two-dimensional turbulence. Phys Fluids 12(12):233–239. https://doi.org/10.1063/1.1692443

Boffetta G (2007) Energy and enstrophy fluxes in the double cascade of two-dimensional turbulence. J Fluid Mech 589:253–260. https://doi.org/10.1017/S0022112007008014

Boffetta G, Ecke RE (2012) Two-dimensional turbulence. Annu Rev Fluid Mech 44(1):427–451. https://doi.org/10.1146/annurev-fluid-120710-101240

Brumer SE, Zappa CJ, Anderson SP, Dugan JP (2016) Riverine skin temperature response to subsurface processes in low wind speeds. J Geophys Res 121(3):1721–1735. https://doi.org/10.1002/2015JC010746

Buckley MP, Veron F, Yousefi K (2020) Surface viscous stress over wind-driven waves with intermittent airflow separation. J Fluid Mech 905:31. https://doi.org/10.1017/jfm.2020.760

Chickadel CC, Talke SA, Horner-Devine AR, Jessup AT (2011) Infrared-based measurements of velocity, turbulent kinetic energy, and dissipation at the water surface in a tidal river. IEEE Geosci Remote Sens Lett 8(5):849–853. https://doi.org/10.1109/LGRS.2011.2125942

Dingemans MW (1997) Water wave propagation over uneven bottoms: (in 2 parts). In: Advanced Series on Ocean Engineering, vol. 13. World Scientific Publishing Company. http://www.worldscientific.com/worldscibooks/10.1142/1241

Donelan MA (1987) The effect of swell on the growth of wind waves. J Hopkins APL Tech Dig 8(1):18–23
Donelan MA, Babanin AV, Young IR, Banner ML (2006) Wave-follower field measurements of the wind-input spectral function part II: Parameterization of the wind input. J Phys Oceanogr 36(8):1672–1689. https://doi.org/10.1175/JPO2933.1
Downing HD, Williams D (1975) Optical constants of water in the infrared. J Geophys Res 80(12):1656–1661. https://doi.org/10.1029/JC080i012p01656
Dugan JP, Piotrowski CC (2012) Measuring currents in a coastal inlet by advection of turbulent eddies in airborne optical imagery. J Geophys Res 117:03020. https://doi.org/10.1029/2011JC007600
Fairall CW, Bradley EF, Rogers DP, Edson JB, Young GS (1996) Bulk parameterization of air-sea fluxes for tropical ocean-global atmosphere coupled-ocean atmosphere response experiment. J Geophys Res Oceans 101(C2):3747–3764. https://doi.org/10.1029/95JC03205
Gemmrich JR, Farmer DM (2004) Near-surface turbulence in the presence of breaking waves. J Phys Oceanogr 34(5):1067–1086
Guerra M, Thomson J (2017) Turbulence measurements from five-beam acoustic doppler current profilers. J Atmos Oceanic Tech 34(6):1267–1284. https://doi.org/10.1175/JTECH-D-16-0148.1
Guo X, Shen L (2010) Interaction of a deformable free surface with statistically steady homogeneous turbulence. J Fluid Mech 658:33–62. https://doi.org/10.1017/S0022112010001539
Guo X, Shen L (2013) Numerical study of the effect of surface waves on turbulence underneath. Part 1. Mean flow and turbulence vorticity. J Fluid Mech 733:558–587. https://doi.org/10.1017/jfm.2013.451
Handler RA, Smith GB, Leighton RI (2001) The thermal structure of an air-water interface at low wind speeds. Tellus A Dyn Meteorol Oceanogr 53(2):233. https://doi.org/10.3402/tellusa.v53i2.12187
Hogan L, Zappa CJ, Cifuentes-Lorenzen A, Edson JB, O'Donnell J, Ullman DS (2025) Observations of breaking wave dissipation and their relationship to atmosphere? Ocean energy transfer. J Geophys Res Oceans 130(6):2024–022130. https://doi.org/10.1029/2024JC022130
Jiang J, Street RL (1991) Modulated flows beneath wind? Ruffled, mechanically generated water waves. J Geophys Res Oceans 96(C2):2711–2721. https://doi.org/10.1029/90JC02259
Kawai S (1982) Structure of air flow separation over wind wave crests. Bound-Layer Meteorol 23(4):503–521. https://doi.org/10.1007/BF00116275
Kline SJ, Reynolds WC, Schraub FA, Runstadler PW (1967) The structure of turbulent boundary layers. J Fluid Mech 30(4):741–773. https://doi.org/10.1017/S0022112067001740
Kraichnan RH (1967) Inertial ranges in two-dimensional turbulence. Phys Fluids 10(7):1417–1423. https://doi.org/10.1063/1.1762301
Kraichnan RH (1971) Inertial-range transfer in two- and three-dimensional turbulence. J Fluid Mech 47(3):525–535. https://doi.org/10.1017/S0022112071001216
Laxague NJM, Zappa CJ (2020) Observations of mean and wave orbital flows in the ocean's upper centimetres. J Fluid Mech 887:10. https://doi.org/10.1017/jfm.2019.1019
Leibovich S (1977) On the evolution of the system of wind drift currents and Langmuir circulations in the ocean. Part 1. Theory and averaged current. J Fluid Mech 79(4):715–743. https://doi.org/10.1017/S002211207700041X
Leibovich S (1980) On wave-current interaction theories of Langmuir circulations. J Fluid Mech 99(4):715–724. https://doi.org/10.1017/S0022112080000857
Leibovich S, Paolucci S (1980) The Langmuir circulation instability as a mixing mechanism in the upper ocean. J Phys Oceanogr 10(2):186–207
Leibovich S, Radhakrishnan K (1977) On the evolution of the system of wind drift currents and Langmuir circulations in the ocean part 2 structure of the Langmuir vortices. J Fluid Mech 80(3):481–507. https://doi.org/10.1017/S0022112077001803
Lindborg E (1999) Can the atmospheric kinetic energy spectrum be explained by two-dimensional turbulence? J Fluid Mech 388:259–288. https://doi.org/10.1017/S0022112099004851
Mascheck (1979) Phillips, O. M., The Dynamics of the Upper Ocean. 2. Edition, Cambridge-London-New York-Melbourne. Cambridge University Press. 1977. 336 S., £ 16.00 A. ZAMM - J Appl. Math. Mech. Zeitschrift für Angewandte Mathematik und Mechanik 59(7), 331–332. https://doi.org/10.1002/zamm.19790590714. Accessed 27 Feb 2025
Mcwilliams JC (1984) The emergence of isolated coherent vortices in turbulent flow. J Fluid Mech 146:21–43. https://doi.org/10.1017/S0022112084001750
McWILLIAMS JC, Sullivan PP, Moeng C-H (1997) Langmuir turbulence in the ocean. J Fluid Mech 334:1–30. https://doi.org/10.1017/S0022112096004375
Méhauté B (1976) An introduction to hydrodynamics and water waves. Springer, Berlin Heidelberg. https://doi.org/10.1007/978-3-642-85567-2
Melville WK, Shear R, Veron F (1998) Laboratory measurements of the generation and evolution of Langmuir circulations. J Fluid Mech 364:31–58. https://doi.org/10.1017/S0022112098001098
Noh Y, Min HS, Raasch S (2004) Large Eddy simulation of the ocean mixed layer: the effects of wave breaking and Langmuir circulation. J Phys Oceanogr 34(4):720–735
Okuda K (1982) Internal flow structure of short wind waves. J Oceanogr Soc Jpn 38(1):28–42. https://doi.org/10.1007/BF02113819
Pope SB (2000) Turbulent flows, 1st edn. Cambridge University Press, Cambridge. https://doi.org/10.1017/CBO9780511840531
Rascle N, Nouguier F, Chapron B, Mouche A, Ponte A (2016) Surface roughness changes by finescale current gradients: properties at multiple azimuth view angles. J Phys Oceanogr 46(12):3681–3694. https://doi.org/10.1175/JPO-D-15-0141.1
Rashidi M, Hetsroni G, Banerjee S (1992) Wave-turbulence interaction in free-surface channel flows. Phys Fluids A 4(12):2727–2738. https://doi.org/10.1063/1.858331
Savelyev I, Fuchs J (2018) Stereo thermal marking velocimetry. Front Mech Eng 4:1. https://doi.org/10.3389/fmech.2018.00001
Savelyev IB, Buckley MP, Haus BK (2020) The impact of nonbreaking waves on wind-driven ocean surface turbulence. J Geophys Res Oceans 12:51. https://doi.org/10.1029/2019JC015573
Shabani B, Ware P, Baldock TE (2022) Suppression of wind waves in the presence of swell: a physical modeling study. J Geophys Res Oceans 127(5):2021–018306. https://doi.org/10.1029/2021JC018306
Siddiqui K, Loewen MR (2010) Phase-averaged flow properties beneath microscale breaking waves. Bound-Layer Meteorol 134(3):499–523. https://doi.org/10.1007/s10546-009-9447-6
Skyllingstad ED, Denbo DW (1995) An ocean large? Eddy simulation of Langmuir circulations and convection in the surface mixed layer. J Geophys Res Oceans 100(C5):8501–8522. https://doi.org/10.1029/94JC03202
Soloviev A, Lukas R (2003) Observation of wave-enhanced turbulence in the near-surface layer of the ocean during TOGA COARE. Deep Sea Res Part I 50(3):371–395. https://doi.org/10.1016/S0967-0637(03)00004-9
Sullivan PP, McWilliams JC (2010) Dynamics of winds and currents coupled to surface waves. Annu Rev Fluid Mech 42(1):19–42. https://doi.org/10.1146/annurev-fluid-121108-145541
Sullivan PP, McWILLIAMS JC, Melville WK (2007) Surface gravity wave effects in the oceanic boundary layer: large-eddy simulation with vortex force and stochastic breakers. J Fluid Mech 593:405–452. https://doi.org/10.1017/S002211200700897X

Sutherland P, Melville WK (2015) Measuring turbulent kinetic energy dissipation at a wavy sea surface. J Atmos Oceanic Tech 32(8):1498–1514. https://doi.org/10.1175/JTECH-D-14-00227.1
Tabeling P (2002) Two-dimensional turbulence: a physicist approach. Phys Rep 362(1):1–62. https://doi.org/10.1016/S0370-1573(01)00064-3
Teixeira MAC (2018) A model for the wind-driven current in the wavy oceanic surface layer: apparent friction velocity reduction and roughness length enhancement. J Phys Oceanogr 48(11):2721–2736. https://doi.org/10.1175/JPO-D-18-0086.1
Teixeira MAC, Belcher SE (2002) On the distortion of turbulence by a progressive surface wave. J Fluid Mech 458:229–267. https://doi.org/10.1017/S0022112002007838
Tenhaus J, Buckley MP, Matt S, Savelyev IB (2024) Viscous and turbulent stress measurements above and below laboratory wind waves. Exp Fluids 65(12):174. https://doi.org/10.1007/s00348-024-03898-7
Terray EA, Donelan MA, Agrawal YC, Drennan WM, Kahma KK, Williams AJ, Hwang PA, Kitaigorodskii SA (1996) Estimates of kinetic energy dissipation under breaking waves. J Phys Oceanogr 26(5):792–807
Thais L, Magnaudet J (1996) Turbulent structure beneath surface gravity waves sheared by the wind. J Fluid Mech 328:313–344. https://doi.org/10.1017/S0022112096008749
Thomson J (2012) Wave breaking dissipation observed with "swift" drifters. J Atmos Oceanic Tech 29(12):1866–1882. https://doi.org/10.1175/JTECH-D-12-00018.1
Veron F, Melville WK (2001) Experiments on the stability and transition of wind-driven water surfaces. J Fluid Mech 446:25–65
Veron F, Melville WK, Lenain L (2008) Infrared techniques for measuring ocean surface processes. J Atmos Oceanic Tech 25(2):307–326. https://doi.org/10.1175/2007JTECHO524.1
Veron F, Melville WK, Lenain L, Veron F, Melville WK, Lenain L (2009) Measurements of ocean surface turbulence and wave-turbulence interactions. J Phys Oceanogr 39(9):2310–2323. https://doi.org/10.1175/2009JPO4019.1
Wiles PJ, Rippeth TP, Simpson JH, Hendricks PJ (2006) A novel technique for measuring the rate of turbulent dissipation in the marine environment. Geophys Res Lett 33(21):2006–027050. https://doi.org/10.1029/2006GL027050
Xiao Z, Wan M, Chen S, Eyink GL (2009) Physical mechanism of the inverse energy cascade of two-dimensional turbulence: a numerical investigation. J Fluid Mech 619:1–44. https://doi.org/10.1017/S0022112008004266
Zappa CJ, Asher WE, Jessup AT (2001) Microscale wave breaking and air? Water gas transfer. J Geophys Res 106(2000):9385–9391. https://doi.org/10.1029/2000JC000262
Zappa CJ, Asher WE, Jessup AT (2001) Microscale wave breaking and air-water gas transfer. J Geophys Res 106(2000):9385–9391. https://doi.org/10.1029/2000JC000262
Zappa CJ, McGillis WR, Raymond PA, Edson JB, Hintsa EJ, Zemmelink HJ, Dacey JWH, Ho DT (2007) Environmental turbulent mixing controls on air-water gas exchange in marine and aquatic systems. Geophys Res Lett. https://doi.org/10.1029/2006GL028790
Zappa CJ, Banner ML, Schultz H, Corrada-Emmanuel A, Wolff LB, Yalcin J (2008) Retrieval of short ocean wave slope using polarimetric imaging. Meas Sci Technol 19(5):055503. https://doi.org/10.1088/0957-0233/19/5/055503